G-quadruplexes

Expanding the Toolbox of Target Directed Bio-Orthogonal Synthesis: *In Situ* Direct Macrocyclization by DNA Templates

Ritapa Chaudhuri, Thumpati Prasanth, and Jyotirmayee Dash*

Dedicated to Professor Ayyappanpillai Ajayagosh on his 60th birthday

Abstract: Herein, we demonstrate for the first time that noncanonical DNA can direct macrocyclization-like challenging reactions to synthesize gene modulators. The planar G-quartets present in DNA G-quadruplexes (G4s) provide a size complementary reaction platform for the bio-orthogonal macrocyclization of bifunctional azide and alkyne fragments over oligo- and polymerization. G4s immobilized on gold-coated magnetic nanoparticles have been used as target templates to enable easy identification of a selective peptidomimetic macrocycle. Structurally similar macrocycles have been synthesized to understand their functional role in the modulation of gene function. The innate fluorescence of the *in situ* formed macrocycle has been utilized to monitor its cellular localization using a G4 antibody and its *in cell* formation from the corresponding azide and alkyne fragments. The successful execution of *in situ* macrocyclization *in vitro* and in cells would open up a new dimension for target-directed therapeutic applications.

Introduction

Target-guided synthesis (TGS) has emerged as a powerful tool for identifying target-selective leads without prior synthesis and high-throughput screening.[1–3] It has been efficiently used for the facile synthesis of inhibitors for various therapeutic proteins as well as ribonucleoprotein targets.[4–7] However, DNA/RNA targets as templates remain less explored for the design and development of small molecules for modulating gene function.[8–11] The Dervan group first employed duplex DNA as a template to conjugate two minor groove-binding anti-parallel hairpin polyamides by azide-alkyne cycloaddition, demonstrating its

[*] R. Chaudhuri, T. Prasanth, Dr. J. Dash
School of Chemical Sciences, Indian Association for the Cultivation of Science, 2A and 2B Raja S.C. Mullick Road, Jadavpur, Kolkata 700099 (India)
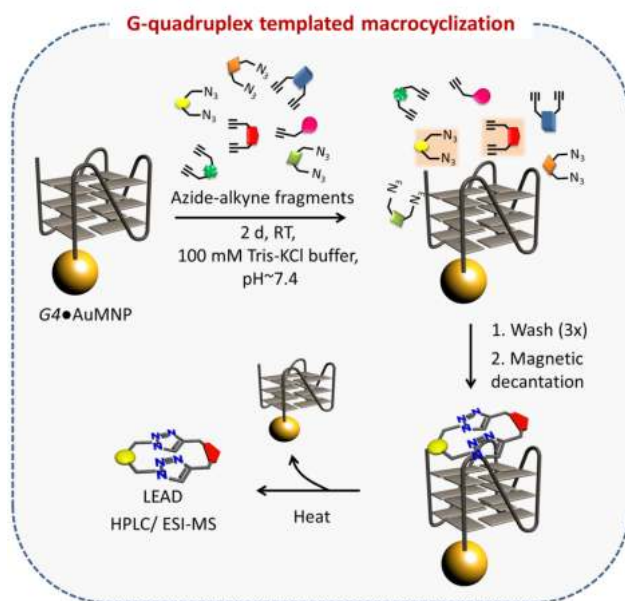E-mail: ocjd@iacs.res.in
Homepage: http://iacs.res.in/faculty-profile.html?id=98

T. Prasanth
Department of Medicinal Chemistry, National Institute of Pharmaceutical Education and Research Kolkata
Chunilal Bhawan,168, Maniktala Main Road, P.O. Bengal Chemicals, P.S. Phoolbagan, Kolkata 700054 (India)

feasibility for specific genome targeting.[12] Balasubramanian and co-workers explored noncanonical DNA/RNA G-quadruplexes (G4s) as templates to discover their high-affinity binders.[13,14] Herein, we delineate the *target-directed macrocyclization* of bifunctional building blocks to generate a new class of peptidomimetic macrocycles using G4s as targets. Owing to the structural constraints of peptide and peptidomimetic macrocycles, they exhibit metabolic stability and enhanced binding affinity for biomolecular targets.[15] The large surface area of peptidomimetic macrocycles prevents intercalative binding to double-stranded DNA and shows selectivity towards DNA quadruplexes.[10,16–19] However, the synthesis of macrocycles, especially ring-closing reactions, is always cumbersome and challenging. The azide-alkyne cycloaddition has been utilized as a tool for the construction of macrocyclic scaffolds that find applications in peptide and carbohydrate chemistry, supramolecular systems and medicinal chemistry.[6,20–22]

Double cycloaddition between bifunctional fragments leading to macrocyclization requires high dilution conditions, often undergoes polymerization and is unachievable at high temperatures.[15,23] The target-guided synthesis of peptides such as macrocyclic ligands by *in situ* double click reaction would not only enable the efficient construction of macrocyclic structures but also assist in identifying the binders of a biological target without synthesizing all of them. However, the identification of *in situ*-generated ligands from the reaction mixture has always been challenging. In this work, we present that G4s could selectively guide the synthesis of a macrocyclic peptidomimetic from a pool of bis-alkyne and bis-azide fragments (Scheme 1). This macrocyclic ligand has also been synthesized in live cells from its corresponding fragments and shows a promising biological profile.

Tetrahelical DNA G4s are abundantly present in the telomeric region of chromosomes and the promoter region of oncogenes.[24,25] Small molecule-mediated G4 stabilization has been considered an evolving approach for modulating gene expression as well as maintaining telomere length.[26–29] Since G4s contain a G-quartet having a cyclic structure as the basic structural motif, we thus presumed that the G4 DNA targets could template the formation of macrocyclic binders of similar size among the indefinite possibilities of generating linear open chain products as well.

Scheme 1. Schematic representation of the target-guided synthesis of G4-selective ligands by DNA-functionalized magnetic gold nanoparticles.

Results and Discussion

To generate target-specific ligands, we have prepared a pool of 6 bis-alkynes (**1a–f**) and 9 mono/bis-azides (**2a–i**) containing aliphatic, aromatic, and carboxamide functional groups as well as alkyl amine side chains (Figure 1a–b). These bifunctional azide-alkyne building blocks would bind to the adjacent sites of G4 DNA templates and lower the energy of the system generating products that bind to the target by noncovalent interactions.

Thiolated sequences of *c-MYC*, *h-TELO*, *c-KIT1*, *c-KIT2*, *BCL2* G4 DNAs and a *ds*DNA has been used as DNA templates for instant covalent tethering on gold-coated magnetic nanoparticles (AuMNPs) (Scheme 1). The attachment of DNAs with the nanoparticles was confirmed by the characteristic surface plasmon resonance (SPR) peak of Au at 540 nm and the DNA peak at 260 nm in the UV/Vis spectrum in 100 mM Tris-KCl buffer, pH ~ 7.4 (Figure S1–S2). Circular Dichroism (CD) spectroscopy revealed that *c-MYC, c-KIT1, c-KIT2, BCL2* and *h-TELO* G4s immobilized on Au-MNPs exhibited characteristic CD signatures and retained their G4 conformations (Figure S3).

The multicomponent reaction was conducted in a single pot consisting of 6 bis-alkynes (**1a–f**) and 9 mono/bis-azides (**2a–i**) (in a 1:3 ratio) with a particular G4 DNA (*c-MYC/c-KIT1/c-KIT2/BCL2/h-TELO*) or a *ds*-DNA immobilized on
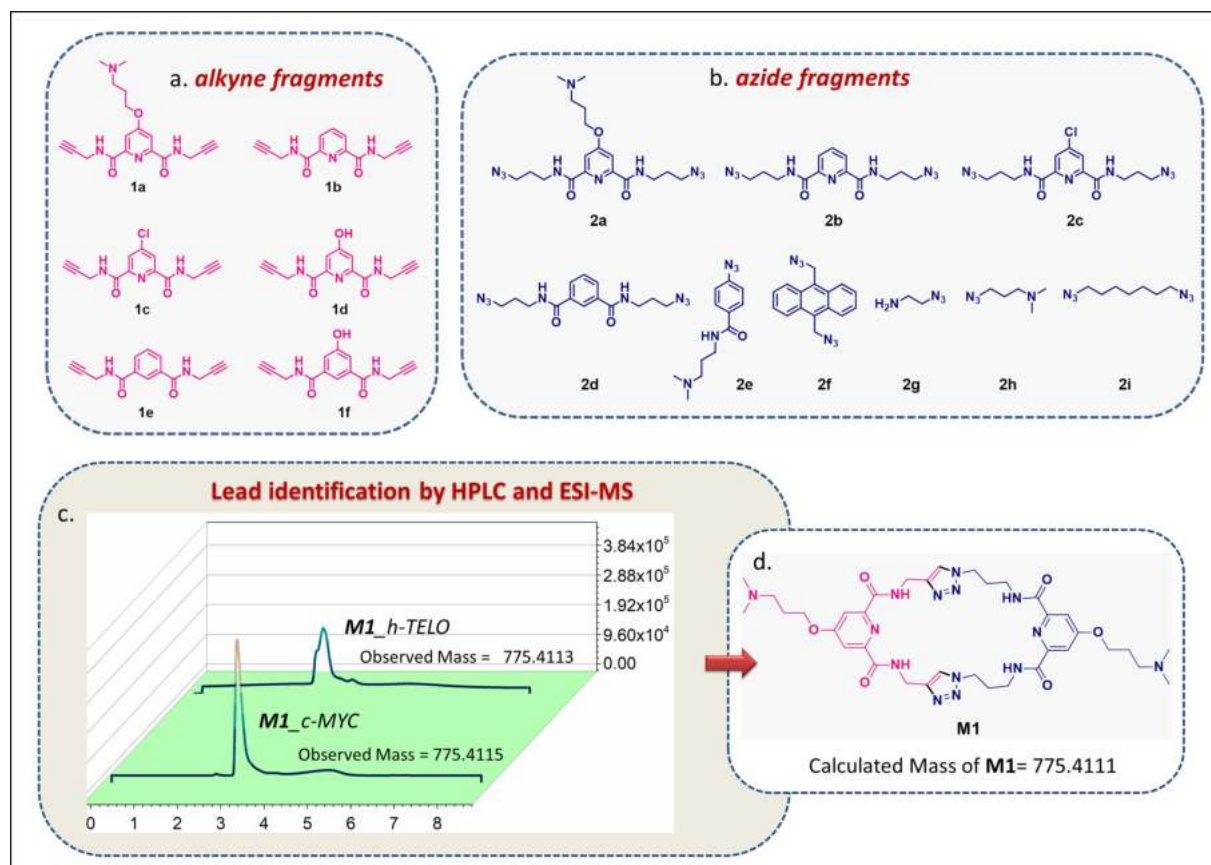

Figure 1. G4 nanotemplate-directed *in situ* cycloaddition. a) Structures of alkyne building blocks (**1a–f**). b) Structures of azide building blocks (**2a–i**). c) HPLC chromatograms of the *in situ* formed macrocyclic ligand by *c-MYC* and *h-TELO* nanotemplates. d) Structure of **M1**.

Angew. Chem. Int. Ed. **2023**, e202215245 (2 of 8)

© 2022 Wiley-VCH GmbH

AuMNPs in Tris-KCl buffer (100 mM), pH ~ 7.4 at 4°C. Each reaction was carried out for 24 h as well as 48 h by constant stirring to avoid precipitation of the nanoparticles. The unreacted azides and alkynes from each reaction mixture were separated by magnetic decantation. Next, G4-AuMNPs were thoroughly washed 3 times with Tris-KCl buffer (100 mM, pH ~ 7.4) to remove unreacted and loosely bound ligands. Thus, only the most selective and strongly bound ligands would sustain this selection process. The mixture was then heated at 65°C for 5 min to unfold the G4 DNA so that the ligands could be released into the solution. The DNA was then separated by magnetic decantation, and the solution mixture was analyzed by HPLC, followed by ESI-MS for the identification of the products formed by the *in situ* reaction.

After 48 h, *c-MYC* G4-AuMNPs generated bis-triazolyl macrocyclic ligand **M1**. The same product was also obtained by the *h-TELO* G4-AuMNPs (Figure 1c–d, Figure S4).

The relative yield of the macrocycle **M1** was determined to be higher for the *c-MYC* (26% more) than the *h-TELO* template as obtained from the area under the peak in the HPLC chromatogram (Figure S5). However, the formation of **M1** was not detected after stirring the reaction for 24 h.

No product was detected from the TGS reactions carried out in the presence of *c-KIT1*, *c-KIT2*, *BCL2* and *ds*DNA even after 48 h. Although all G4s contain G-quartet-like topology, this observation infers that the G4 topology plays a crucial role in templating the *in situ* reaction. To date, only a few macrocyclic ligands, such as telomestatin,[30] HXDV,[31,32] TmPyP4,[33] Se2SAP[34] etc.[17,35–39] are known for targeting DNA quadruplexes.

To determine the regioselectivity of the *in situ*-generated **M1**, we synthesized **M1** by standard Cu[I]-catalyzed azide-alkyne cycloaddition (CuAAC) under high dilution conditions (Figure 2a). It was observed that both the *in situ* and Cu[I]-catalyzed reactions yielded the 1,4 disubstituted *anti*-triazole regioisomer (Figure S4).

To understand the binding properties of this class of macrocycles, we further synthesized 3 more structurally similar compounds, **M2**, **M3** and **M4**, by Cu[I]-catalyzed azide-alkyne cycloaddition (CuAAC) (Figure 2a–b and Scheme S1). Although the formation of the macrocycle **M4** from components **1b** and **2b** was not detected by the G4-directed synthesis, we synthesized **M4** to understand the role of the macrocyclic core and the side chains for G4 interactions. The reactions of pyridine bis-carboxamide
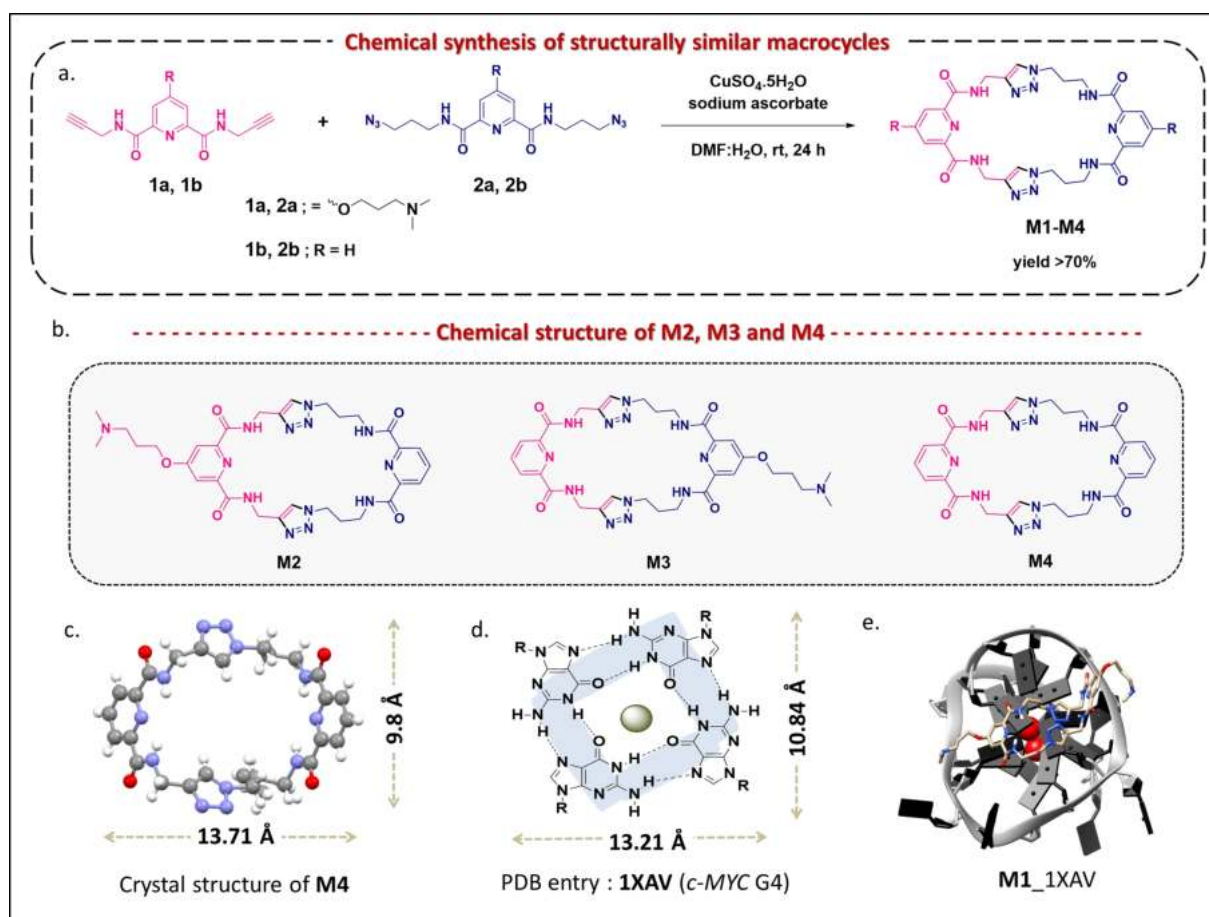

Figure 2. a) Chemical synthesis of macrocycles (**M1–M4**) by Cu[I]-catalyzed azide-alkyne cycloaddition. b) Structure of **M2**, **M3** and **M4**. c) Crystal structure of **M4**. d) Selected dimensions of a G-quartet (obtained from X-ray structure; PDB entry: 1XAV). e) Docked structure of **M1** with *c-MYC* G4 DNA (PDB entry: 1XAV).

containing bis-azides (**2a**, **2b**) with bis-alkynes bearing pyridine bis-carboxamide (**1a**, **1b**) were carried out using catalytic $CuSO_4.5H_2O$ (0.6 eq.) and sodium ascorbate (0.8 eq.) in DMF-H_2O to obtain bis-triazole macrocycles **M1**–**M4** in high yields (70–78%) (Figure 2a–b and Scheme S1). This class of macrocycles containing 4 amide bonds and two amide bond isosteres (triazole motifs) could act as potential therapeutic peptidomimetic ligands for intracellular targets.

The structure of **M4** was confirmed by single crystal X-ray analysis (CCDC number- 2150728,[40] Figure 2c, and Figure S6 and Table S1). It was observed that the dimension of the macrocyclic core (~13.7 Å × 9.8 Å) is similar to the dimension of the G-quartet geometry (13.6 Å × 10.9 Å; calculated using Gauss view and VMD packages[41]) (Figure 2c–d). Owing to such precise geometric complementarity and large surface area of the macrocyclic cores of the macrocycles (as **M1**–**M4**), they are anticipated to exhibit selectivity towards G4 DNAs. Moreover, the crystal structure shows that each 2,6-pyridine biscarboxamide unit in **M4** is interlocked *via* intramolecular hydrogen bonding between pyridine nitrogen and amide N–H bonds (Figure S7). The importance of such structural parameters of bisquinolinium and pyridostatin ligands for the selective G4 recognition has previously been demonstrated.[42,43]

The binding interactions of **M1**–**M4** with different types of quadruplex structures (*c-KIT1*, *c-KIT2*, *c-MYC*, *BCL-2*, *k-RAS*, *h-TELO*) were evaluated using biophysical and biological studies.

A high throughput FRET-based melting assay using double labelled (5′ FAM - 3′ TAMRA) G4 sequences *c-MYC, BCL2, c-KIT1, c-KIT2, k-RAS, h-TELO*) and a control duplex-DNA was performed to analyze the G4 stabilization potential of the peptidomimetic macrocycles (Figures 3a and 3b, Table S2 and Figure S8–12). The FRET-based melting assay revealed that ligands **M1** and **M2** substantially stabilized the *c-MYC* ($T_m \sim 66°C$) and *h-TELO* ($T_m \sim 46°C$) quadruplexes in a dose-dependent manner. **M1** displayed a ΔT_m of 10°C and 20°C for the *c-MYC* and 7.7°C and 39°C for the *h-TELO* G4 DNAs at 1 and 5 μM conc., respectively. Similarly, **M2** exhibited a ΔT_m of 12.8°C and 15.6°C for the *c-MYC* and 6.6°C and 26°C for the *h-TELO* G4 DNAs at 1 and 5 μM conc., respectively (Figure 3a and 3b, Figure S9–S10). Surprisingly, **M3**, having one side chain on the pyridine opposite to **M2**, did not show any significant stabilization potential (0–6.6°C; 0–5 μM conc.) for any of the quadruplexes (Figure S11). Macrocycle **M4**, lacking side chains, also showed weak stabilization potential (0–8.8°C; 0–5 μM conc.) for most of the investigated quadruplexes (Figure S12). This infers the important role of the side chains of this class of macrocyclic scaffolds for G4 interactions. As expected, none of the macrocyclic ligands **M1**–**M4** stabilized *ds*DNA (Figure S8). The corresponding alkyne **1a** and azide **2a** fragments of **M1** showed very weak stabilization potential with ΔT_m values ~2–0.8°C at 5 μM concentrations (Table S2). Moreover, a FRET-based competition assay (Figure S13) suggested high specificity of the macrocycles **M1** and **M2** for G4s over duplex DNA as negligible changes in the T_m values of the studied G4s,
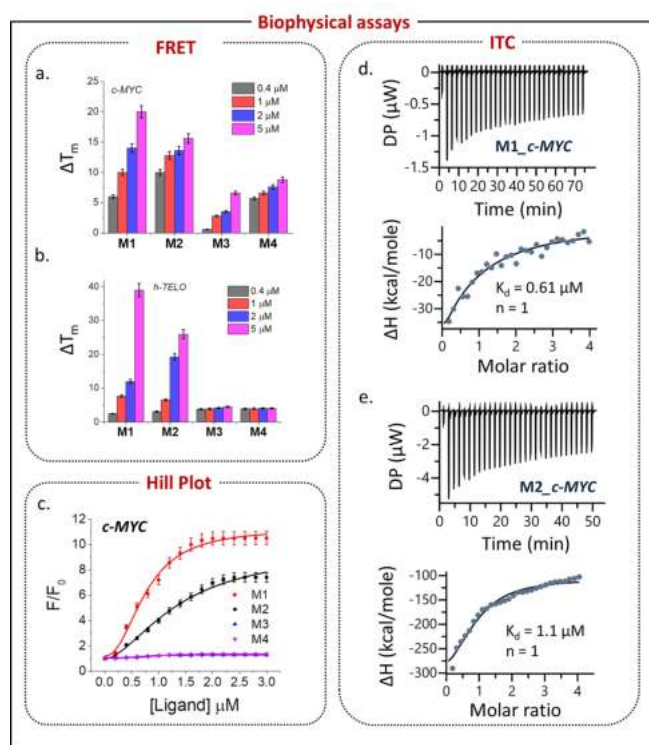

Figure 3. FRET-melting analysis of *c-MYC* and *h-TELO* G4s in the presence of increasing amounts of a) **M1** and b) **M2** (0.4–5 μM) in 60 mM K^+- cacodylate buffer, pH ~ 7.4. The T_m values of the quadruplexes in 60 mM K^+ - cacodylate buffer, pH ~ 7.4, in the absence of ligands are *c-MYC* (66 ± 1), *BCL2* (74 ± 1), *c-KIT1* (60 ± 1), *c-KIT2* (51 ± 1), *k-RAS* (52 ± 1), *h-TELO* (46 ± 1) *ds* DNA (76 ± 1) °C; maximum measurable $T_m = 95°C$. c) Fluorescence response curves of macrocyclic ligands **M1**–**M4** with *c-MYC* G4 DNA in 100 mM Tris-KCl buffer, pH ~ 7.4. ITC titration profiles of 2.5 μM *c-MYC* with 25 μM d) **M1** and e) **M2**

induced by the macrocycles (1 μM) were observed in the presence of 100 times excess of competitor *ds*DNA (20 μM).

The binding affinities (K_d) of the ligands towards different G4s were determined by fluorometric titration (Figure S14–S17). The fluorescence intensity of **M1** increased by ~9-fold ($K_d = 0.9$ μM) upon incremental addition of *c-MYC* G4 DNA, while its spectral intensity remained unchanged upon titration with *ds*DNA. Interestingly, **M2** also exhibited a comparably high binding affinity ($K_d \sim 1.2$ μM) for *c-MYC* G4 with an 8-fold enhancement of spectral intensity. The emission intensities of **M1** and **M2** were increased by 4-fold ($K_d \sim 7.3$ μM) and 5.4-fold ($K_d \sim 5.4$ μM), respectively, upon the addition of *h-TELO* G4. This observation indicates that although both ligands bind to *h-TELO*, they exhibit a comparatively higher binding affinity for *c-MYC* (Figure 3c). Ligands **M3** and **M4**, with similar cyclic cores, did not show much specificity or affinity for *c-MYC* in comparison to **M1** and **M2**. Consistent with the TGS results (that did not generate **M4**), **M4** exhibited nonspecific and weak binding towards *c-MYC*, *c-KIT2* and *h-TELO* G4s. This trend suggests that macrocyclic ligands **M1** and **M2**, with the side chain on the pyridine ring derived from the alkyne fragment, show higher binding affinity towards G4s than **M3** (side

chain on the pyridine ring derived from the azide unit) or **M4** without any side chain.

We next performed isothermal titration calorimetry (ITC) to explore the thermodynamic characterization of the binding reactions (Figure S18–S19 and Table S3). Both **M1** and **M2** showed exothermic reactions (negative ΔH) with *c-MYC* and *h-TELO* G4 DNA. However, they exhibited less favourable endothermic reactions with other quadruplexes, indicating a lack of strong interaction (hydrogen bond) with the target.[44] **M1** and **M2** showed a maximum binding affinity for *c-MYC* G4 DNA, having K_d values of 0.6 µM and 1.1 µM (Figure 3d–e), respectively, with a 1:1 binding stoichiometry. In agreement with fluorimetric titration, **M1** and **M2** displayed comparatively lower binding affinities of ~3.3 µM and ~2.6 µM for *h-TELO*, respectively. Both fluorescence and ITC studies revealed that these ligands displayed negligible binding with duplex DNA.

Molecular modelling studies further show that ligand **M1** attains a flat but flexible conformation in the presence of *c-MYC* G4 (Figure 2e), although the macrocyclic core is nonplanar, as observed from the crystal structure. The model further delineates that the two triazoles and one pyridine ring are positioned for optimal interaction with the G-quartet surface, while the amine flanking side arms participate in electrostatic interaction with the G4 loops and grooves, enabling the macrocyclic ring to stack upon the top of the G-quartet (Figure 2e). Molecular docking of ligand **M2** with *c-MYC* G4 revealed that the macrocyclic core interacts with the G-quartet, while one side chain interacts with the phosphate backbone (Figure S20). Despite having a similar ring size, a subtle chemical change in the side chains plays a pivotal role in molecular recognition. Both **M2** and **M3** peptidomimetic macrocycles having similar cores with one side chain showed differential binding affinity and specificity for quadruplexes. The amine side chain present in the alkyne fragment in **M1** showed high binding affinities compared to **M2** having a side chain in the opposite pyridine ring (i.e., side chain in the azide fragment). CD spectroscopy studies revealed that the *c-MYC* G4 retains its conformation even in the presence of 15 mole equivalent of macrocycles (**M1–M4**) (Figure S21).

Next, the cytotoxicity of **M1**, **M2**, **M3** and **M4** was examined against a cervical cancer cell line (HeLa) as well as a normal kidney epithelial (NKE) cell line using the XTT assay. Ligands **M1** and **M2** showed IC_{50} values of 5.7 ± 0.28 µM and 8.5 ± 0.43 µM, respectively, in HeLa cells. Ligands **M3** and **M4** exhibited similar cytotoxicities, with IC_{50} values of 8.9 ± 0.44 µM and 7.6 ± 0.38 µM, respectively (Figure S22, Table S4). However, all of them showed less toxicity for normal NKE cells ($IC_{50} > 60$ µM). Flow cytometric analysis using an apoptotic marker (Annexin V and PI) revealed that **M1** induced apoptosis in 61 % of the cell population and necrosis in 10.8 % of the cell population. **M2** also induced apoptosis in 45 % and necrosis in 8.7 % of the cell population (Figure S23).

The *in vitro* effect of the ligands **M1–M4** on the expression of the *c-MYC* gene relative to the expression of housekeeping genes was investigated in HeLa cells by qRT-PCR and western blot (Figure 4a–c and Figure S24). After 24 h of treatment, **M1** reduced the *c-MYC* expression to 0.62-fold (by 38 %) and 0.24-fold (by 76 %) at 2.5 µM and 5 µM concentrations, respectively (Figure 4a). Similarly, **M2** also lowered the *c-MYC* mRNA expression to 0.70-fold (by 30 %) and to 0.38-fold (by 62 %) at 2.5 and 5 µM concentrations, respectively. **M3** and **M4** did not show any significant effect in lowering the *c-MYC* mRNA expression. Western blot assay of cell lysates collected after 24 h of treatment with **M1** and **M2** revealed their ability to silence *c-MYC* expression in a dose-dependent manner. The *c-MYC* protein expression was lowered by 49 % and by 65 % by **M1** and by 9 % and 32 % by **M2** at 2.5 µM and 5 µM concentrations, respectively (Figure 4b–c). These results suggest that **M1** represses *c-MYC* expression more efficiently than **M2** at the transcriptional and translational levels without altering the expression of housekeeping genes.

Dual luciferase assay performed by co-transfection of firefly luciferase reporter vector (Del4) containing the wild-type or mutant *c-MYC* quadruplex-forming sequence in its promoter region along with Renilla luciferase vector (pGL3), having a non-G4 promoter in HeLa cells revealed 51 % and 40 % reduction of *c-MYC*-promoter-linked luciferase expression by **M1** and **M2**, respectively, at 5 µM concentration (Figure 4d). However, neither **M1** nor **M2** altered luciferase expression in the *c-MYC* mutant promoter (unable to form the G4 structure), indicating that the observed downregulation of *c-MYC* expression is triggered by quadruplex stabilization (Figure S25). Immunofluorescence was carried out using the G4-specific antibody BG4, that shows scattered punctate (red) nuclear staining indicating the presence of G4s in cells.[45] The blue fluorescence of **M1** confirmed its nuclear localization and a 2.6 fold increase in BG4 foci in **M1** treated Hela cells relative to the untreated control (Figure S26–S27) further established its binding to G4 DNAs in HeLa cells (Figure 4e).

A few interesting instances of copper-free bioorthogonal *in cell* click reactions have been delineated for the identification of subcellular localization, cell transplantation, tumor-specific drug delivery, etc.[46–49] The efficient *in situ* macrocyclization motivated us to explore its feasibility in cells *via* a copper-free click reaction of azides and alkynes. ESI-MS analysis of cell extracts following treatment with 2.5 µM **1a** and **2a** (starting fragments, $IC_{50} > 50$ µM) in Hela cells for 48 h revealed *m/z* values corresponding to **M1** indicating *in cell* macrocyclization along with unreacted **1a** and **2a** (Figure S28). Treatment of cells with **1a** and **2a** also increased the BG4 foci by ~2 fold, suggesting the intracellular formation of **M1** that subsequently stabilizes and traps the endogenous G-quadruplex structures (Figure S29). However, the cells treated separately with **1a** and **2a** did not show an increase in the number of BG4 foci relative to the untreated control. The results thus support that the endogenous G4s templates the macrocyclization yielding **M1** that binds and stabilizes G4 structures in cancer cells. In order to eliminate the possibility of formation of **M1** as a result of molecular crowding or the presence of trace amounts of copper(I) in the cells, the macrocyclization reaction of **1a** and **2a** has been carried out in nucleic acid free cell extracts. The absence of *m/z* value corresponding to
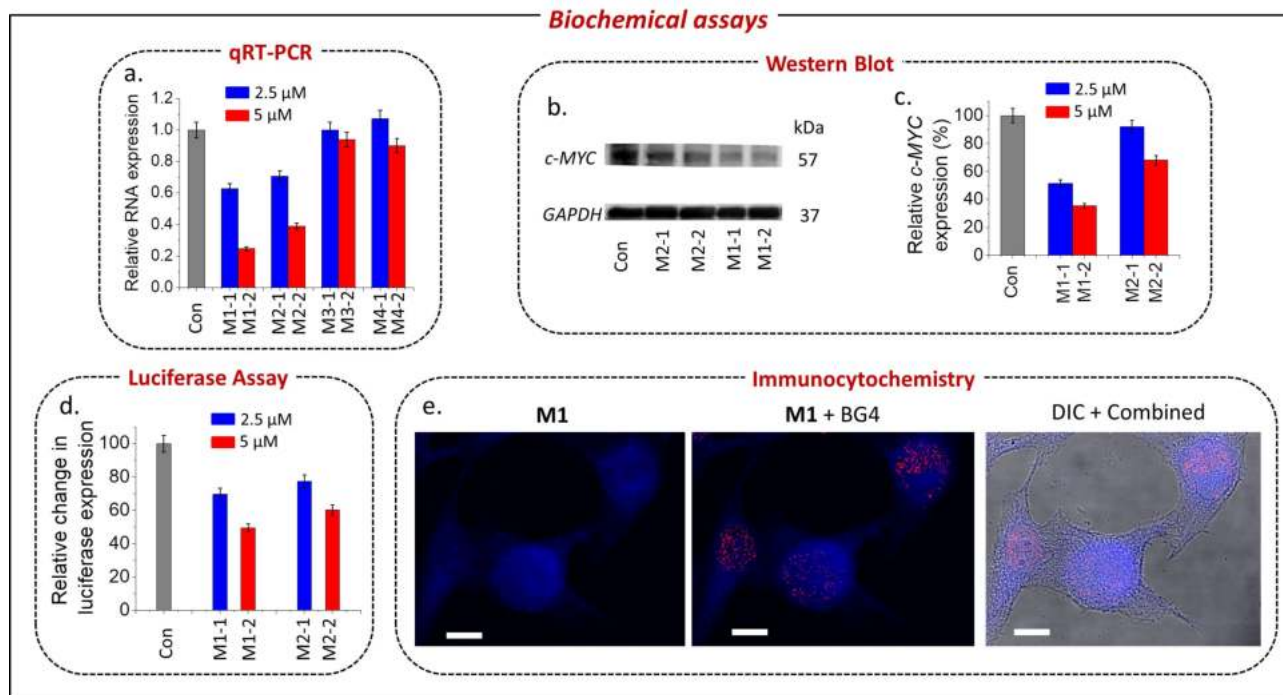
Figure 4. a) qRT-PCR for *c-MYC* in HeLa cells after treatment with DMSO (control) and 2.5 and 5 µM **M1**–**M4** for 24 h. b) Western blot bands of *c-MYC* and GAPDH proteins obtained upon treatment with ligand **M1** and **M2** at 2.5 and 5 µM concentrations in HeLa cells. c) Bar diagram representing dose-dependent downregulation of *c-MYC* protein by 2.5 and 5 µM of **M1** and **M2**. d) The relative luciferase expression in the *c-MYC* promoter containing firefly plasmid normalized with pRL-TK Renilla plasmid (FF/RL) upon treatment with 2.5 and 5 µM **M1** and **M2** in HeLa cells. Data shown here are the mean SD; $P < 0.05$. e) Immunocytochemistry showing nuclear localization of **M1** (2.5 µM) and an increase in BG4 foci number after treatment with **M1** in HeLa cells, imaged with a Leica DMI8 Stellaris 5 microscope, scale bars, 10 µm.

M1 in ESI-MS analysis indicated that the endogenous G-quadruplexes played a crucial role in templating the macro-cyclization reaction in cells (Figure S30).

Next, the effect of the *in cell* formed macrocyclic ligand **M1** on transcriptional regulation has been investigated (Figure S31). Alkyne **1a** did not significantly change the *c-MYC* mRNA expression; however, a reduction in expression (0.7-fold, 30 %) was observed when cells were treated with **2a** at a 2.5 µM concentration for 48 h, possibly due to nonspecific interaction of the positively charged amine group of **2a** with the negatively charged phosphate back-bone of the DNA. Interestingly, when cells were treated with both **1a** and **2a**, a substantial decrease in mRNA expression (0.25-fold, at 48 h) was observed, compared to the change in expression of *c-MYC* upon treatment with **M1** (0.65-fold at 48 h and 0.62-fold 24 h at 2.5 µM concentration). The combined treatment of **1a** and **2a** exhibited more profound effect in reducing *c-MYC* expression, compared to **M1**, again corroborating the *in cell* formation of **M1**, which in combination with the free **2a** exert a cumulative effect on *c-MYC* mRNA expression.

Conclusion

In summary, we have accomplished the first DNA-templated synthesis of a peptidomimetic macrocycle (**M1**) by harnessing the power of noncovalent interactions. This study showcases macrocyclization-like challenging reaction can be achieved using target directed synthetic approach. Structural analogues of **M1** have also been synthesized by Cu$^{\mathrm{I}}$-catalyzed cycloaddition. The comparison of the crystal structure of the G-quadruplex and one of the macrocyclic ligands illuminates that complementary structural motif plays a crucial role in the formation of high affinity macro-cyclic peptidomimetics through irreversible bond formation between bis-azide and bis-alkyne fragments. In this work, G-quadruplexes have been used as the model templates, other biomolecular templates such as RNA, ribonucleoprotein or proteins having flat undruggable surfaces can be employed to generate high affinity macrocyclic ligands. The *in situ* formed ligand exhibited excellent binding and stabilization of G4 DNA and also demonstrated G4-mediated gene silencing in cancer cells. Moreover, it has been demonstrated that macrocyclization reactions can also occur in G4-over-expressing cancer cells. The *in cell*-generated product (**M1**), along with its unreacted azide and alkyne fragments efficiently suppressed gene expression. Thus, the functional groups in alkyne and azide fragments can be tuned to generate specific chemical probes for intracellular targeting and imaging without the need for their prior synthesis. This previously unexplored strategy would inspire *in situ* and *in cell* macrocyclization as fascinating approaches for chemical intervention against clinically relevant targets.

Conflict of Interest

The authors declare no conflict of interest.

Data Availability Statement

The data that support the findings of this study are available in the supplementary material of this article.

[1] W. G. Lewis, L. G. Green, F. Grynszpan, Z. Radić, P. R. Carlier, P. Taylor, M. Finn, K. B. Sharpless, *Angew. Chem. Int. Ed.* **2002**, *41*, 1053–1057; *Angew. Chem.* **2002**, *114*, 1095–1099.

[2] N. Z. Fantoni, A. H. El-Sagheer, T. Brown, *Chem. Soc. Rev.* **2021**, *121*, 7122–7154.

[3] A. Bhardwaj, J. Kaur, M. Wuest, F. Wuest, *Nat. Commun.* **2017**, *8*, 1.

[4] X. Jin, S. S. Daher, M. Lee, B. Buttaro, R. B. Andrade, *ACS Med. Chem. Lett.* **2018**, *9*, 907–911.

[5] T. Hirose, N. Maita, H. Gouda, J. Koseki, T. Yamamoto, A. Sugawara, H. Nakano, S. Hirono, K. Shiomi, T. Watanabe, *Proc. Natl. Acad. Sci. USA* **2013**, *110*, 15892–15897.

[6] W. Xu, Y. H. Lau, G. Fischer, Y. S. Tan, A. Chattopadhyay, M. de la Roche, M. Hyvönen, C. Verma, D. R. Spring, L. S. Itzhaki, *J. Am. Chem. Soc.* **2017**, *139*, 2245–2256.

[7] I. Glassford, C. N. Teijaro, S. S. Daher, A. Weil, M. C. Small, S. K. Redhu, D. J. Colussi, M. A. Jacobson, W. E. Childers, B. Buttaro, *J. Am. Chem. Soc.* **2016**, *138*, 3136–3144.

[8] D. Panda, P. Saha, T. Das, J. Dash, *Nat. Commun.* **2017**, *8*, 16103.

[9] T. Bhattacharyya, D. Panda, J. Dash, *Org. Lett.* **2021**, *23*, 3004–3009.

[10] M. Yasuda, Y. Ma, S. Okabe, Y. Wakabayashi, D. Su, Y. T. Chang, H. Seimiya, M. Tera, K. Nagasawa, *Chem. Commun.* **2020**, *56*, 12905–12908.

[11] S. G. Rzuczek, H. Park, M. D. Disney, *Angew. Chem. Int. Ed.* **2014**, *53*, 10956–10959; *Angew. Chem.* **2014**, *126*, 11136–11139.

[12] A. T. Poulin-Kerstien, P. B. Dervan, *J. Am. Chem. Soc.* **2003**, *125*, 15811–15821.

[13] M. Di Antonio, G. Biffi, A. Mariani, E. A. Raiber, R. Rodriguez, S. Balasubramanian, *Angew. Chem. Int. Ed.* **2012**, *51*, 11073–11078; *Angew. Chem.* **2012**, *124*, 11235–11240.

[14] M.-H. Hu, X. Chen, S.-B. Chen, T.-M. Ou, M. Yao, L.-Q. Gu, Z.-S. Huang, J.-H. Tan, *Sci. Rep.* **2015**, *5*, 13174.

[15] V. Martí-Centelles, M. D. Pandey, M. I. Burguete, S. V. Luis, *Chem. Rev.* **2015**, *115*, 8736–8834.

[16] A. Granzhan, D. Monchaud, N. Saettel, A. Guédin, J. L. Mergny, M. P. Teulade-Fichou, *J. Nucleic Acids* **2010**, *2010*, 525862.

[17] A. Granzhan, D. Monchaud, N. Saettel, A. Guédin, J. L. Mergny, M. P. Teulade-Fichou, *J. Nucleic Acids* **2010**, *2010*, 460561.

[18] C. Heinis, *Nat. Chem. Biol.* **2014**, *10*, 696–698.

[19] A. Isidro-Llobet, T. Murillo, P. Bello, A. Cilibrizzi, J. T. Hodgkinson, W. R. Galloway, A. Bender, M. Welch, D. R. Spring, *Proc. Natl. Acad. Sci. USA* **2011**, *108*, 6793–6798.

[20] V. K. Tiwari, B. B. Mishra, K. B. Mishra, N. Mishra, A. S. Singh, X. Chen, *Chem. Rev.* **2016**, *116*, 3086–3240.

[21] Y. H. Lau, Y. Wu, M. Rossmann, B. X. Tan, P. de Andrade, Y. S. Tan, C. Verma, G. J. McKenzie, A. R. Venkitaraman, M. Hyvönen, *Angew. Chem. Int. Ed.* **2015**, *54*, 15410–15413; *Angew. Chem.* **2015**, *127*, 15630–15633.

[22] D. A. Heller, Y. Levi, J. M. Pelet, J. C. Doloff, J. Wallas, G. W. Pratt, S. Jiang, G. Sahay, A. Schroeder, J. E. Schroeder, *Adv. Mater.* **2013**, *25*, 1449–1454.

[23] D. Pasini, *Molecules* **2013**, *18*, 9512–9530.

[24] R. Hänsel-Hertsch, M. Di Antonio, S. Balasubramanian, *Nat. Rev. Mol. Cell Biol.* **2017**, *18*, 279–284.

[25] J. Spiegel, S. Adhikari, S. Balasubramanian, *Trends Chem.* **2020**, *2*, 123–136.

[26] M.-H. Hu, T.-Y. Wu, Q. Huang, G. Jin, *Nucleic Acids Res.* **2019**, *47*, 10529–10542.

[27] W. Long, B.-X. Zheng, Y. Li, X.-H. Huang, D.-M. Lin, C.-C. Chen, J.-Q. Hou, T.-M. Ou, W.-L. Wong, K. Zhang, *Nucleic Acids Res.* **2022**, *50*, 1829–1848.

[28] J. Dickerhoff, J. Dai, D. Yang, *Nucleic Acids Res.* **2021**, *49*, 5905–5915.

[29] F. Ilaria, P. Valentina, R. N. Sara, D. Filippo, *Int. J. Biol. Macromol.* **2022**, *204*, 89–102.

[30] M. Y. Kim, H. Vankayalapati, K. Shin-Ya, K. Wierzba, L. H. Hurley, *J. Am. Chem. Soc.* **2002**, *124*, 2098–2099.

[31] G. S. Minhas, D. S. Pilch, J. E. Kerrigan, E. J. LaVoie, J. E. Rice, *Bioorg. Med. Chem. Lett.* **2006**, *16*, 3891–3895.

[32] C. M. Barbieri, A. R. Srinivasan, S. G. Rzuczek, J. E. Rice, E. J. LaVoie, D. S. Pilch, *Nucleic Acids Res.* **2007**, *35*, 3272–3286.

[33] A. Siddiqui-Jain, C. L. Grand, D. J. Bearss, L. H. Hurley, *Proc. Natl. Acad. Sci. USA* **2002**, *99*, 11593–11598.

[34] J. Seenisamy, S. Bashyam, V. Gokhale, H. Vankayalapati, D. Sun, A. Siddiqui-Jain, N. Streiner, K. Shin-Ya, E. White, W. D. Wilson, *J. Am. Chem. Soc.* **2005**, *127*, 2944–2959.

[35] M. Tera, H. Ishizuka, M. Takagi, M. Suganuma, K. Shinya, K. Nagasawa, *Angew. Chem. Int. Ed.* **2008**, *47*, 5557–5560; *Angew. Chem.* **2008**, *120*, 5639–5642.

[36] Y. Ma, K. Iida, S. Sasaki, T. Hirokawa, B. Heddi, A. T. Phan, K. Nagasawa, *Molecules* **2019**, *24*, 263.

[37] E. S. Baker, J. T. Lee, J. L. Sessler, M. T. Bowers, *J. Am. Chem. Soc.* **2006**, *128*, 2641–2648.

[38] P. S. Shirude, E. R. Gillies, S. Ladame, F. Godde, K. Shin-Ya, I. Huc, S. Balasubramanian, *J. Am. Chem. Soc.* **2007**, *129*, 11890–11891.

[39] P. Maleki, Y. Ma, K. Iida, K. Nagasawa, H. Balci, *Nucleic Acids Res.* **2017**, *45*, 288–295.

[40] Deposition number 2150728 (for **M4**) contains the supplementary crystallographic data for this paper. These data are provided free of charge by the joint Cambridge Crystallographic Data Centre and Fachinformationszentrum Karlsruhe Access Structures service (see also the Supporting Information).

[41] W. Humphrey, A. Dalke, K. Schulten, *J. Mol. Graphics* **1996**, *14*, 33–38.

[42] S. Müller, D. A. Sanders, M. Di Antonio, S. Matsis, J. F. Riou, R. Rodriguez, S. Balasubramanian, *Org. Biomol. Chem.* **2012**, *10*, 6537–6546.

[43] A. De Cian, E. DeLemos, J. L. Mergny, M. P. Teulade-Fichou, D. Monchaud, *J. Am. Chem. Soc.* **2007**, *129*, 1856–1857.

[44] K. K. Frederick, M. S. Marlow, K. G. Valentine, A. J. Wand, *Nature* **2007**, *448*, 325–329.

[45] G. Biffi, D. Tannahill, J. McCafferty, S. Balasubramanian, *Nat. Chem.* **2013**, *5*, 182–186.

[46] P. Parvatkar, N. Kato, M. Uesugi, S. I. Sato, J. Ohkanda, *J. Am. Chem. Soc.* **2015**, *137*, 15624–15627.

[47] A. Battigelli, B. Almeida, A. Shukla, *Bioconjugate Chem.* **2022**, *33*, 263–271.

[48] M. L. Smeenk, J. Agramunt, K. M. Bonger, *Curr. Opin. Chem. Biol.* **2021**, *60*, 79–88.

[49] Y. Takayama, K. Kusamori, M. Nishikawa, *Molecules* **2019**, *24*, 172.

Research Articles

G-quadruplexes

R. Chaudhuri, T. Prasanth,
J. Dash* —————————— **e202215245**

Expanding the Toolbox of Target Directed
Bio-Orthogonal Synthesis: *In Situ* Direct
Macrocyclization by DNA Templates
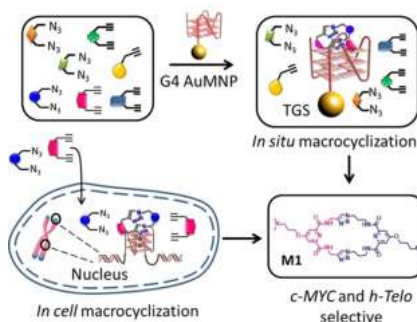
This work demonstrates the first instance of bioorthogonal macrocyclization directed by non-canonical DNAs as templates. The size complementarity of the macrocyclic core with the G-quartet of a G-quadruplex DNA plays a key role to drive the macrocyclization over oligomerization. *In cellulo* macrocyclization has also been established leading to a peptidomimetic macrocycle with promising therapeutic properties.

Bioconjugate Chemistry

Article

Thiazole Containing PNA Mimic Regulates *c-MYC* Gene Expression through DNA G-Quadruplex

Ananta Gorai,[‡] Ritapa Chaudhuri,[‡] Titas Kumar Mukhopadhyay, Ayan Datta, and Jyotirmayee Dash*

Cite This: *Bioconjugate Chem.* 2022, 33, 1145−1155

Read Online

ACCESS | Metrics & More | Article Recommendations | Supporting Information

ABSTRACT: Peptide nucleic acids (PNAs), besides hybridizing to complementary DNA and RNAs, bind and stabilize DNA secondary structures. Herein, we illustrate the design and synthesis of PNA-like scaffolds by incorporating five-membered thiazole rings as modified bases instead of nucleobases and their subsequent effects on gene regulation by biophysical and *in vitro* assays. A thiazole-modified PNA trimer selectively recognizes *c-MYC* G-quadruplex (G4) DNA over other G4s and duplex DNA. It displays a high stabilization potential for the *c-MYC* G4 DNA and shows remarkable fluorescence enhancement with the *c-MYC* G4. It is flexible enough to bind at 5′ and 3′ ends as well as in the groove region of *c-MYC* G4. Furthermore, the PNA trimer easily permeates the cellular membrane and suppresses *c-MYC* mRNA expression in HeLa cells by targeting the promoter G4. This study illuminates modified PNAs as flexible molecular tools for selective targeting of noncanonical nucleic acids and modulating gene function.
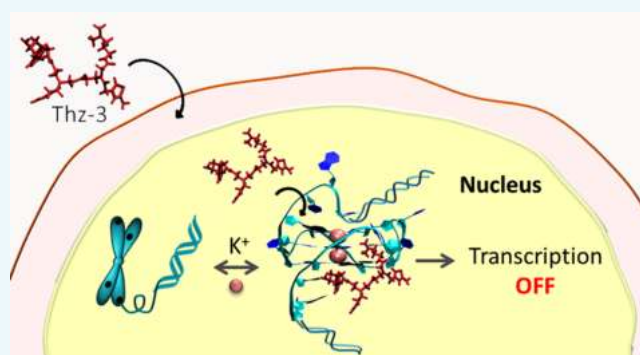
INTRODUCTION

PNAs are synthetic analogues of natural nucleic acids that can undergo complementary base pairing with themselves as well as DNA or RNA by Watson−Crick base pairing.[1,2] The peptide backbone of PNA, in place of the sugar−phosphate backbone of DNA, renders them unrecognizable by cellular enzymes like nucleases and proteases.[3] Interestingly, despite having an achiral backbone and neutral charge, PNAs exhibit strand invasion properties[4−6] and sequence fidelity. The structural uniqueness and integrity of PNA makes them stable at acidic and basic conditions as well as high temperatures. PNAs have been initially developed for hybridization to duplex DNA for a higher thermodynamic stability of PNA−DNA duplexes compared to DNA−DNA duplexes. Various PNA oligomers have been reported to recognize noncanonical DNA/RNA G-quadruplexes (G4) by forming heteroduplexes or heteroquadruplexes.[7−10] Phan et al. reported that guanine-linked PNA can stabilize a particular G4 by dual recognition.[11] Panyutin and co-workers illustrated short PNA oligomers can induce *BCL2* G4 formation using C-strand-invading short PNAs.[12] Recently, Richter et al. reported naphthalene diimide ligand-conjugated PNA for selectively targeting the G4 present in the HIV-1 LTR region.[13] However, PNA, like ligands for directly targeting G4s, remains less explored.[14]

In spite of many advantages, the major limitation is that unmodified PNAs lack efficient cell penetration.[15,16] Strategies like base modification or incorporation of suitable motifs have been developed to render PNAs cell-permeable. For instance, introduction of 2-aminopyridine as the nucleobase in triplex-forming PNAs or incorporation of guanidine groups to the PNA backbone led to increased stability as well as cellular permeation.[17] It has been shown that conjugation of cell-penetrating peptides like Tat peptides[18] or addition of arginine or lysine side chains[19] to PNAs stimulated their cellular permeation like naturally occurring proteins.[20] However, there is evidence of accumulation of peptide conjugated PNAs in the endosomes resulting in decreased functional activities.[21]

Here, we delineate the synthesis of PNA-like ligands by replacing the nucleobases with amino-thiazole moieties for enhanced cell permeability. The thiazole ring is a unique five-membered heterocyclic privileged scaffold, present in numerous cyclic peptidomimetics as well as biologically active natural products.[22,23] Thiazole-modified PNAs could adopt flexible conformations and directly bind to a particular noncanonical G4 DNA by hydrogen bonding interactions.

G4 DNA sequences are predominant at the telomeric end, at the promoter regions of the proto-oncogenes, as well as in the untranslated regions of mRNAs.[24−27] The promoter region (NHE III[1]) of *c-MYC* oncogene harbors a G4 forming region that regulates 85−90% of *c-MYC* gene expression.[28−31] The
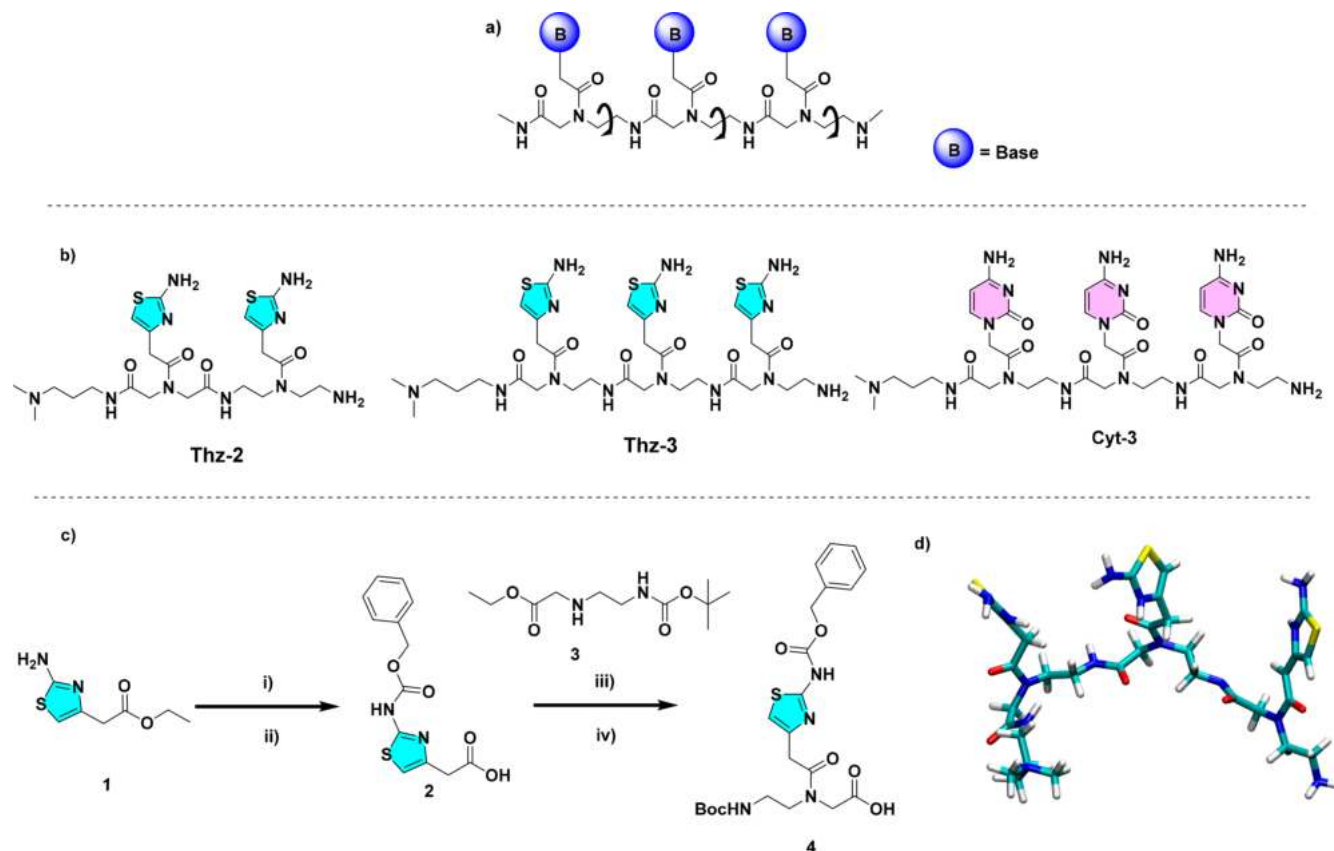
Scheme 1. (a) Structure of Base Modified PNA with Freely Rotatable C−C Bonds. (b) Structure of Thiazole Modified PNAs (Thz-2 and Thz-3) and Cytidine Trimer PNA (Cyt-3). (c) Synthesis of Thiazole Modified PNA Monomer 4: (i) CbzCl, DMAP, Dry CH$_2$Cl$_2$. (ii) a. 2 (N) NaOH, 1.5 h. b. 2 (N) HCl, 0 °C. (iii) HBTU, Dry DMF, Dry Et$_3$N, Overnight. (iv) LiOH-H$_2$O, THF-MeOH-H$_2$O (3:3:1). (d) DFT Optimized Structure of Thz-3

stabilization of *c-MYC* G4 using small molecules has been considered a promising approach to downregulate *c-MYC* expression.[32−34] However, a majority of G4 ligands exhibit an extended aromatic system and mostly interact by π−π stacking and electrostatic interactions. Such ligands are unable to distinguish between different G4s present in the genome.

There are specific transcription factors (proteins), present inside cells, that exhibit high specificity for a particular G4 and play a crucial role in gene regulation. We believe that incorporation of thiazole motifs to the PNA backbone could mimic protein−G4 interactions and specifically interact with a particular G4 DNA.

Synthesis of Thiazole Modified PNA Mimic. PNA-like scaffolds, by employing thiazole ring as the modified base, were synthesized by solid-phase peptide synthesis using commercially available reagents (Scheme 1 and Schemes S1−S2, Supporting Information). The thiazole amino acid **1** was first synthesized by refluxing thiourea with α-bromoethyl acetoacetate followed by benzyloxycarbonyl (−CBz) protection and ester hydrolysis (Scheme S1). The amide coupling between thiazole amino acid **2** and PNA backbone **3** (Scheme S2) followed by ester hydrolysis afforded the thiazole-modified PNA monomer unit **4** in moderate yield (Scheme 1c). The PNA monomer **4** was used for the solid-phase synthesis of the dimeric and trimeric PNAs **Thz-2** and **Thz-3**.[35] In order to draw a comparison, we have also synthesized a cytidine PNA trimer **Cyt-3** via solid-phase peptide synthesis.[36] All the compounds are >95% pure as analyzed by HPLC (Figure S1)

The thiazole-modified PNAs could participate in hydrogen bonding with the nucleobases present in G4, and in addition, a protonated PNA could also play a crucial role in electrostatic interactions.

RESULTS AND DISCUSSION

Thz-3 Exhibits Fluorescence Enhancement toward *c-MYC* G4. A fluorimetric titration was carried out to assess the binding affinity of thiazole-modified PNAs and the cytidine PNA with G4s (*c-MYC*, *BCL-2*, *h-TELO*) and ds DNA (Figures S2−S6, Supporting Information). **Thz-3** exhibited very weak intrinsic fluorescence intensity when excited at 300 nm. However, a significant enhancement (a ∼25-fold intensification of fluorescence intensity at 408 nm) was observed upon addition of *c-MYC* G4 DNA (Figure 1a). In contrast, nominal changes in the fluorescence intensity of **Thz-3** were observed upon addition of other DNA quadruplexes (*BCL2*, *h-TELO*). Thus, fluorescence enhancement of **Thz-3** toward *c-MYC* G4 could be utilized for discerning *c-MYC* G4 from duplex DNA as well as among G4 DNAs. In comparison, the fluorescence intensity of **Thz-2** was not altered with *c-MYC* G4 DNA.

The dissociation constant (K_d) of **Thz-3** was determined to be 1.0 μM (Figure 1b) for the *c-MYC* quadruplex, while K_d values for other G4s could not be determined due to weak interactions. These results indicate that **Thz-3** shows a stronger binding affinity for the *c-MYC* G4 as compared to *BCL2* and *h-TELO* quadruplexes (Figure 1b). Further, a G-rich
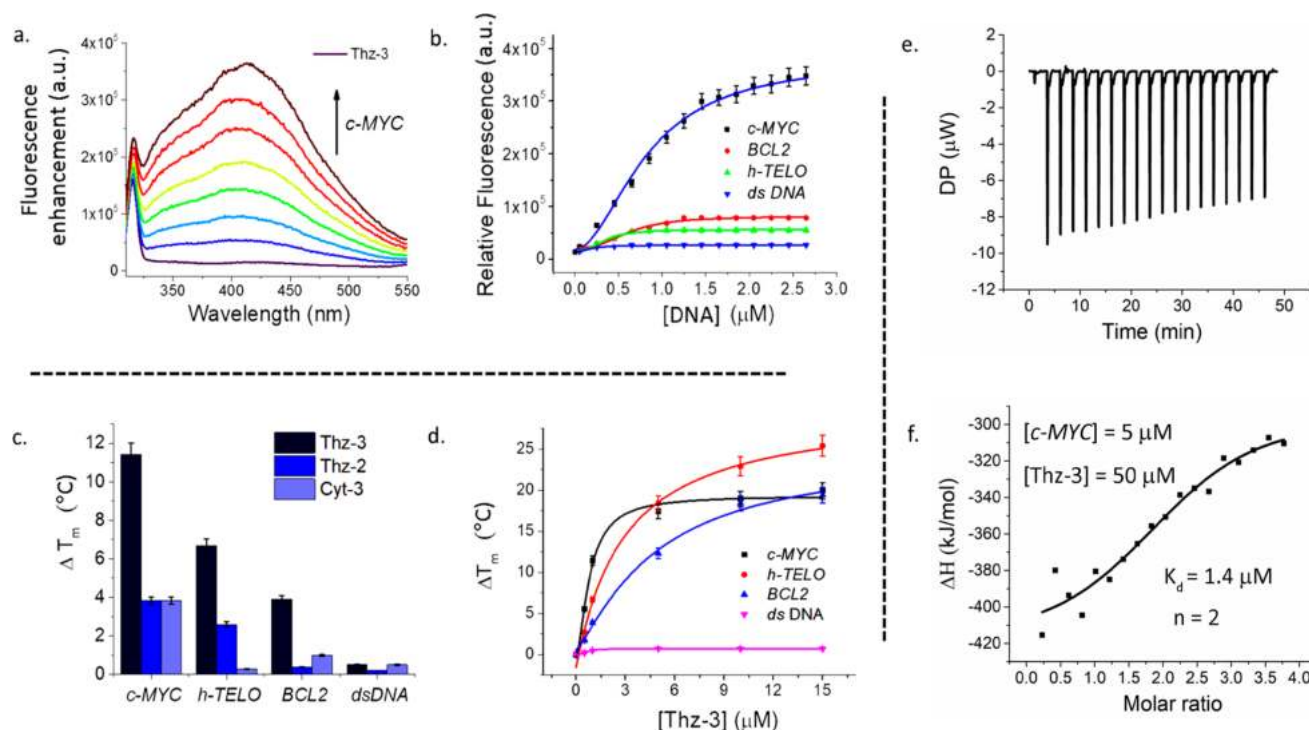
Figure 1. (a) Fluorimetric titration of 0.25 μM of **Thz-3** with ($\sim$0−10 equiv) *c-MYC* G4 DNA in 100 mM Tris-KCl buffer, pH $\sim$ 7.4. (b) Hill plot of **Thz-3** (0.25 μM) titrated with *c-MYC*, *BCL2*, *h-TELO* G4 and *ds* DNA ($\sim$0−10 equiv). (c) Stabilization potential (T_m) of ligands **Thz-3**, **Thz-2**, and **Cyt-3** at 1 μM concentration for *c-MYC* ($T_m \sim$ 75.1 °C), *h-TELO* ($T_m \sim$ 58.6 °C), *BCL2* ($T_m \sim$ 75.6 °C) G4s, and *ds* DNA ($T_m \sim$ 60 °C) in 60 mM K$^+$-cacodylate buffer, pH $\sim$ 7.4, by FRET melting assay. (d) Thermal melting profiles of different G4s and *ds*-DNA (200 nM) upon interaction with **Thz-3** (0−15 μM) in 60 mM K$^+$-cacodylate buffer, pH $\sim$ 7.4. Isothermal calorimetric titration of 5 μM *c-MYC* G4 DNA with 50 μM of **Thz-3** in 100 mM Tris, 100 mM KCl buffer, pH $\sim$ 7.4. (e) raw data showing thermal power required to maintain the isothermal condition between sample and reference cell as a function of time. (f) Binding isotherm showing the ligand concentration normalized heat per peak as a function of the molar ratio.

scrambled *DNA* sequence (*scr*-DNA), unable to fold to a G4, was used to understand the binding specificity of **Thz-3**. Significantly, **Thz-3** did not show any affinity toward *scr*-DNA, indicating its specificity toward a folded G4 structure.

In contrast, **Thz-2** displayed negligible affinity for *c-MYC* as well as *BCL2* (1.2-fold) and *h-TELO* quadruplexes and duplex DNA (1.3-fold). The fluorescence intensity of **Cyt-3** was hardly altered in the presence of G4s (*c-MYC*, *h-TELO*, *BCL2*). These results indicate that the thiazole-modified trimer **Thz-3** binds strongly to *c-MYC* G4 in comparison to dimer **Thz-2** and cytidine PNA trimer **Cyt-3**.

Thz-3 Stabilizes *c-MYC* G4 over Other G4s and *ds* DNA. The stabilization potential of the PNA mimics (**Thz-2**, **Thz-3**, and **Cyt-3**) were analyzed by a Förster Resonance Energy Transfer (FRET)[37,38] melting assay using 5′ FAM and 3′ TAMRA-labeled G4 DNAs and ds DNA. The stabilization potential was quantified by measuring the difference in melting temperature (ΔT_m) of the DNA−PNA complex relative to free G4 DNAs (*BCL2*, *c-MYC*, *h-TELO*) and duplex DNA. PNA trimer **Thz-3** exhibited high stabilization for the *c-MYC* G4 over other quadruplexes and duplex DNA. **Thz-3** showed a ΔT_m value of 11.4 °C ± 0.5 °C (i.e., a T_m of 86.5 °C) for *c-MYC*, 6.7 °C ± 0.3 °C (i.e., a T_m of 65 °C) for *h-TELO*, and 4 °C ± 0.2 °C (i.e., a T_m of 80 °C) for *BCL2* G4 DNA at 1 μM ligand concentration (Figure 1c, Table S1). Both **Thz-2** and **Cyt-3** displayed a weak stabilization potential ($\Delta T_m \sim$ 3.8 °C ± 0.19 °C) for the *c-MYC* G4 while exhibiting an insignificant shift in melting temperature for *h-TELO* and *BCL2* G4s at 1 μM ligand concentration. None of the ligands significantly

altered the melting temperature of *ds* DNA even at a concentration of 15 μM. By increasing the concentration of ligands, it was observed that **Thz-3** could exhibit the maximum measurable stabilization for the *c-MYC* by reaching the melting temperature of 93 °C at 5 μM concentration (Figure 1c).

Thz-2 and **Cyt-3** could not attain the maximum melting temperature values for any of the quadruplexes even at 50 μM concentration (Figures 1d, S7).

Thz-3 Binds Selectively to *c-MYC* G4 Having a Binding Stoichiometry of 1:2. To further validate the observed binding affinity of the modified PNAs with the G4 DNAs, we performed isothermal calorimetry (Figure 1e,f, and Figures S8−10). The binding isotherms obtained after titration of the modified PNAs (50 μM) with G4 DNAs and a control *ds*DNA (5 μM) in 100 mM Tris, 100 mM KCl buffer, pH 7.4, indicated that all the reactions were exothermic in nature. **Thz-3** exhibited a higher binding affinity having a K_d value of $\sim$1.4 μM with *c-MYC* G4 DNA while exhibiting much lower binding affinity (K_d > 12 μM) toward other G4s (*BCL2*, *h-TELO*) and dsDNA. The binding stoichiometry (n) between *c-MYC* G4 and **Thz-3** was found to be 1:2. Binding isotherms obtained upon interaction of **Thz-2** and **Cyt-3** with the G4 DNAs indicated weaker binding interactions with K_d values greater than 7.3 μM (Figures S9, S10, and Table S2). These observations are in good agreement with the binding data observed from the FRET melting assay and fluorimetric titrations.

Further CD analysis was carried out by titrating *c-MYC* G4 DNA (10 μM) with 0−10 equiv of **Thz-2** and **Thz-3**. These
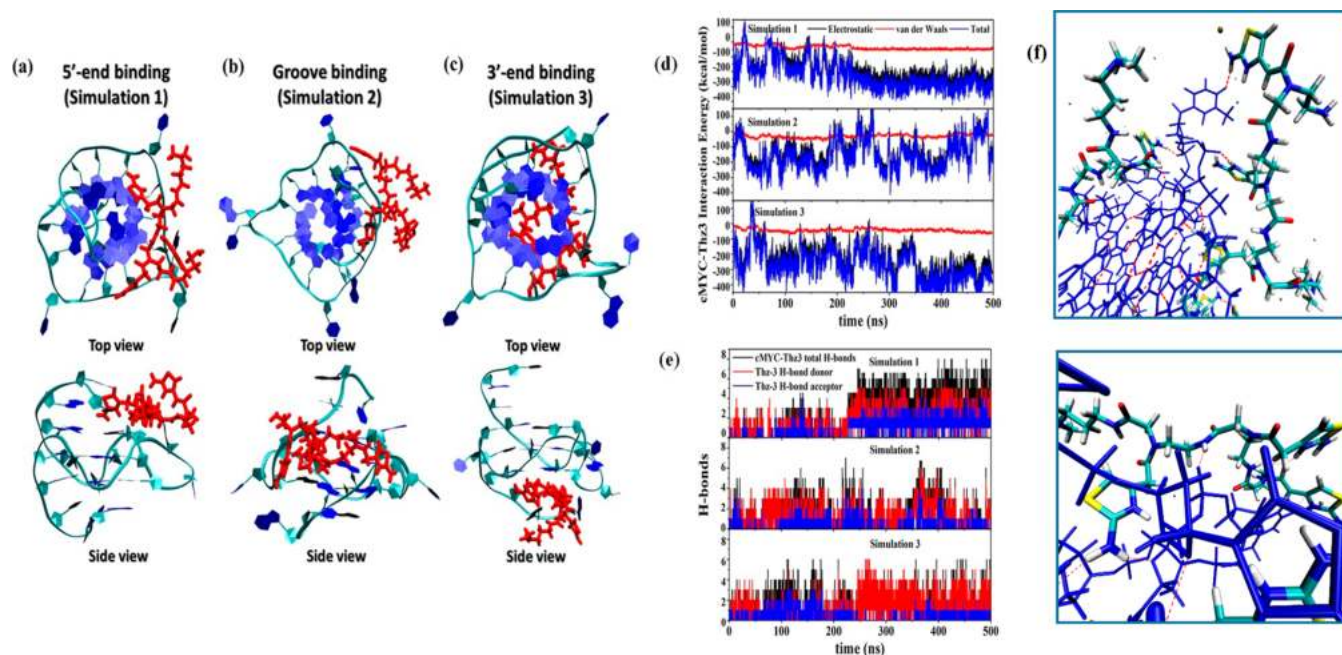
Figure 2. Snapshots from the three independent simulations for the binding of a single **Thz-3** molecule with *c-MYC* G4 DNA demonstrating (a) 5′ end binding (Simulation 1), (b) groove binding (Simulation 2), and (c) 3′ end binding (Simulation 3); time evolution of the dynamic quantities related to the binding of **Thz-3** with *c-MYC*, (d) total interaction energy and decomposition into electrostatic and van der Waals components, (e) total number of H-bonds between *c-MYC* and **Thz-3**, (f) location of H-bonds between **Thz-3** and *c-MYC* G4.

ligands did not significantly affect the secondary structure of *c-MYC* G4 indicating retention of the G4 topology in the presence of the ligands (Figure S11).

Molecular Dynamics Simulation Showing Mechanism of Binding of Thz-3 for *c-MYC* G4. In order to understand the modes of interactions between the *c-MYC* G4 DNA and **Thz-3**, classical molecular dynamics simulations were carried out. Analyses of the simulated trajectories and visual inspection (Figures S12 and S13) revealed that **Thz-3** can bind with *c-MYC* (PDB ID 2L7V)[39] at the 5′ and 3′-terminal tetrads along with the groove region[40−44] of the quadruplex (Figure 2a−c). However, the groove binding mode was quasi-stable, and the bound molecule always searched for a more stable binding position in phase space and tended to move toward the 5′ or 3′ ends. Therefore, when a pool of molecules was available to interact with the *c-MYC*, the **Thz-3** molecules were expected to bind with the quadruplex grooves only after populating the 5′ and 3′ ends. Calculation of the interaction energy (Figure 2d) between the *c-MYC* G4 and **Thz-3** suggested that electrostatic interactions contributed to the majority of the total interaction energy compared to van der Waals interactions. The predominant electrostatic interactions between the molecules were H-bonding and long-range Coulombic interactions, while the contribution from the $\pi-\pi$ stacking and van der Waals interactions was auxiliary. Indeed, in simulations 1 and 3, approximately 5−6 H-bonds were formed between *c-MYC* and **Thz-3**, while in simulation 2, nearly 3−4 H-bonds were formed.

Among these, only 1 H-bond was donated by the quadruplex, while for the rest of the H-bonds, **Thz-3** acted as the donor (Figure 2e). The amino ($-NH_2$) groups present in the thiazole rings and the backbone $-NH-$ groups of **Thz-3** were involved in the donation of H-bonds toward the nucleobases in the capping regions and/or the negatively charged phosphate groups (Figure 2f). The free energy for

binding of the **Thz-3** molecule was calculated to be -10.1 ± 0.2 kcal/mol (Figure S12), which is significant compared to other reported free energies for G4 and small molecule interactions. Further, the simulation of the *c-MYC* G4 with three **Thz-3** molecules unambiguously confirmed that one molecule of **Thz-3** binds at each of the three binding regions of *c-MYC* G-4 DNA, the 5′ end, the 3′ end, and the groove region (Figures S13 and S14), the latter being weaker than the 5′ and 3′ bound states. Interestingly, the 5′ and 3′ end bound structures were stable up to 1500 ns even without any momentary dissociation from the quadruplex and in the major conformation **Thz-3** binds to the 5′ and 3′ ends of *c-MYC* G4 (Figure S15). Therefore, from these observations, a highly stable 1:2 binding stoichiometry between the *c-MYC* and **Thz-3** molecule was concluded, with an additional possibility of quasi-stable groove-binding only if a large excess of **Thz-3** molecules were present. Additionally, upon binding of one or three **Thz-3** molecules, the intra- and inter-tetrad noncovalent interactions were found to be completely preserved, thereby ruling out the possibility of **Thz-3** induced perturbation of the quadruplex native state (Figures S16 and S17). The binding studies revealed that the **Thz-3** could selectively bind and stabilize a G4 structure. The positively charged side chains attached to the PNA could impart electrostatic interactions with the negatively charged phosphate backbone. **Thz-3** contains a heteroaromatic thiazole ring system that can interact with the G-quartet via electrostatic interactions as well as $\pi-\pi$ stacking interactions as observed from MD simulation studies. Consequently, it can interact more efficiently compared to the PNA dimer **Thz-2** due to a higher number of possible interactions. The cytidine trimer **Cyt-3** did not interact with the G4. This indicates that the binding interaction of the PNA is mainly due to thiazole modification.

Antiproliferative Activity of Thz-3 in Cancer Cells. The PNAs **Thz-2**, **Thz-3**, and **Cyt-3** were next evaluated for
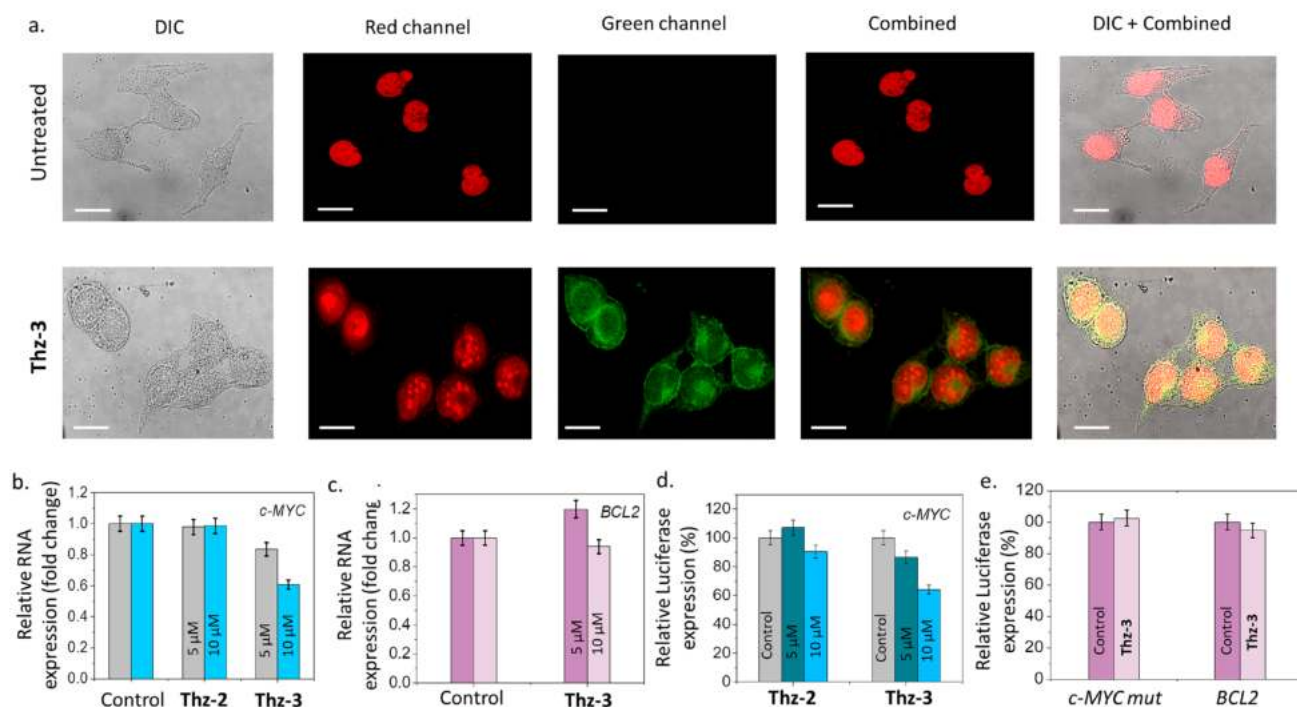
Figure 3. (a) Confocal microscopic images showing untreated and **Thz-3** (5 μM) treated HeLa cells. The nucleus was counterstained with NucRed Live647 ReadyProbe Reagent, for 15 min, and imaged in a Leica DMI8 Stellaris 5 microscope using green and red channels. Scale bar = 20 μm. (b) Transcriptional regulation of *c-MYC* mRNA in the presence of **Thz-2** and **Thz-3** in HeLa cells by qRT-PCR. (c) Bar plot showing relative *BCL2* mRNA expression. (d) Relative luciferase expression of Del4 plasmid containing *c-MYC* promoter upon treatment with **Thz-2** and **Thz-3** after normalization with Renilla luciferase (pRLTK). (e) Relative luciferase expression of Del4 plasmid containing *c-MYC mutant* and *BCL2* promoter upon treatment with 10 μM **Thz-3** after normalization with Renilla luciferase (pRLTK).

their antiproliferative activities in the human cervical cancer (HeLa) cell line and the normal kidney epithelial (NKE) cell line. **Thz-3** exhibited an IC$_{50}$ value of 11.5 μM, while **Thz-2** shows an IC$_{50}$ value of 15 μM in HeLa cells. Both PNAs seemed to have insignificant toxicity toward NKE cells. **Cyt-3** did not exhibit any IC$_{50}$ value in either of the cell lines at a concentration of 20 μM (Figure S18).

Cellular Uptake of Thz-3 in HeLa Cells. The ability of **Thz-3** to penetrate the cellular membrane was assessed by confocal microscopy in HeLa cells (Figure 3a). Confocal imaging was performed by treating HeLa cells with 5 μM **Thz-3** for 24 h. It was observed that **Thz-3** can penetrate the cell membrane and localize into the nucleus (green fluorescence). The colocalization of the commercial dye NucRed with **Thz-3** clearly indicates the binding of **Thz-3** to cellular DNA (Figure 3a). No detectable green fluorescence was observed in untreated HeLa cells stained only with NucRed Live647 ReadyProbe, eliminating the possibility of autofluorescence (Figure 3a). Thus, substituting the nucleic acid bases with identical aminothiazole moieties enabled cellular uptake of the PNA like **Thz-3** ligand. Such observations are consistent with previous reports (only a few) on enhanced cellular permeability of base-modified PNAs compared to unmodified ones.[18,45,46]

Thz-3 Mediated Downregulation of *c-MYC* Expression. The transcriptional arrest by ligands **Thz-2** and **Thz-3** was investigated in HeLa cells (Figures 3b and S20). The *c-MYC* mRNA expression in HeLa cells was determined relative to 18s rRNA expression upon treatment with 5.0 and 10.0 μM of **Thz-2** and **Thz-3**. After 24 h of treatment, the *c-MYC*

mRNA level was significantly reduced to 0.6-fold (i.e., by 40%) by **Thz-3** at 10.0 μM concentration, while no significant reduction in *c-MYC* mRNA expression was observed with **Thz-2** relative to the control cells (treated with 0.1% DMSO). The effect of **Thz-3** on the expression of *BCL2* mRNA was also analyzed (Figures 3c and S21). No significant change in *BCL2* expression was observed, thereby indicating its selectivity toward the *c-MYC* gene.

Thz-3 Modulated *c-MYC* Promoter G4-Dependent Luciferase Expression. Further, the effect on *c-MYC* gene expression as a consequence of *c-MYC* promoter G4 stabilization by the PNAs (**Thz-2** and **Thz-3**) was confirmed by dual luciferase assay (Figure 3d). In this assay, the *c-MYC* Del4 plasmid (promoter containing G4) was cotransfected with the Renilla luciferase plasmid, pRL-TK (promoter without G4), in HeLa cells. The transfected HeLa cells were then treated with 5 μM and 10 μM **Thz-2** and **Thz-3** for 48 h. After normalization with Renilla luciferase expression, **Thz-3** was found to inhibit the *c-MYC* promoter dependent luciferase expression by 64% in comparison to the control cells (Figure 3d). However, negligible changes in the *c-MYC* luciferase expression were observed upon treatment with **Thz-2**.

Furthermore, **Thz-3** was evaluated for its effect on *c-MYC mutant* as well as *BCL2* promoter-driven luciferase plasmids. No significant alteration in luciferase expression relative to Renilla expression for the *c-MYC* mutant and *BCL2* was observed. This further suggests the selectivity of thiazole PNA toward *c-MYC* promoter G4 (Figure 3e).

CONCLUSION

We have synthesized the aminothiazole-subsituted PNA scaffolds **Thz-2** and **Thz-3** as well as a cytidine trimer (**Cyt-3**) to investigate the potential of short PNA mimics for targeting noncanonical DNA G4. Our results show that aminothiazole-substituted PNA-like ligands, particularly **Thz-3**, could inhibit gene expression by selectively interacting with *c-MYC* G4 over other G4s and *ds* DNA. The FRET melting analysis and fluorimetric titration studies collectively indicated **Thz-3** as a potential *c-MYC* G4 DNA binder compared to **Thz-2**. Fluorescence imaging revealed its nuclear localization in HeLa cells. MD simulations further shed light on the possible mode of binding of the **Thz-3** that can interact with one or more guanine residues simultaneously. Moreover, the flexibility of the PNA scaffold allows it to remain in both stretched and folded states, the former being predominant during the 5′ and 3′ end binding while the latter is adopted for groove binding. This study showcases by suitable chemical modifications that the PNA mimic can be designed and explored as flexible molecular and potent drug candidates to target specific biomolecules with promising biological activities.

EXPERIMENTAL SECTION

General Information. All experiments were carried out under an inert atmosphere of argon in flame-dried flasks. Solvents were dried by using standard procedures. All starting materials were obtained from commercial suppliers and used as received. Products were purified by flash chromatography on silica gel (100−200 mesh, Merck). F-moc and Bhoc-protected cytidine monomer (Fmoc-C(Bhoc)-Aeg-OH) was purchased from PolyOrg Inc. Solid-phase peptide synthesis was carried out by using 4-methylbenzhydrylamine (4-MBHA) resin (100−200 mesh size) (0.04−0.09 mmol g^{-1}). ^{1}H NMR spectra were recorded at 500 MHz using Brüker AVANCE 500 MHz and JEOL 400 MHz instruments at 298 K. Signals are quoted as δ values in ppm using residual protonated solvent signals as internal standard (CDCl$_3$: δ = 7.26 ppm, s). Data are reported as follows: chemical shift, multiplicity (s = singlet, d = doublet, t = triplet, q = quartet, b = broad, m = multiplet, and *J* = coupling constants (Hz), integration. ^{13}C NMR spectra were recorded on either a JEOL-400 (100 MHz) or a Brüker ADVANCE 500 MHz (125 MHz) with complete proton decoupling. Chemical shifts (δ) are reported in ppm downfield from tetramethylsilane with the solvent as the internal reference (CDCl$_3$: δ 77.16 ppm). HRMS analyses were performed with Q-TOF YA263 high resolution (Water Corporation) instruments by +ve mode electrospray ionization. All the DNA sequences are brought from Sigma-Aldrich.

General Procedure for CBz Deprotection (GP-1). The Cbz protected ligands (1 equiv) were dissolved in MeOH (2 mL), and then Pd/C catalyst (10 mol %) was added under an atmosphere of argon. The reaction was allowed to stir at room temperature for 6 h under an atmosphere of H$_2$ using a hydrogen balloon. The catalyst was removed by filtration through a pad of Celite, and the solvent was removed under reduced pressure to obtain the corresponding compound in quantitative yield.

Ethyl 2-(2-Aminothiazol-4-yl)acetate (1).[47] α-Bromoethyl-lacetoacetate (5.49 g, 26.3 mmol) was added to a cold solution of thiourea (2.0 g, 26.3 mmol) in dry ethanol (5 mL) in a sealed tube. The resulting mixture was heated for 4 h at 100 °C. Upon cooling to room temperature, the reaction mixture

was poured into ice water and brought to pH ∼ 8 with aqueous sodium carbonate solution. The resulting solid precipitate was filtered, washed with water (3 × 10 mL), and air-dried to obtain pure off-white solid compound **1** (4.15 g, 85%). ^{1}H NMR (400 MHz, DMSO-d_6) δ 6.89 (s, 2H), 6.30 (s, 1H), 4.05 (q, *J* = 7.1 Hz, 2H), 3.44 (s, 2H), 1.17 (t, *J* = 7.1 Hz, 3H). ^{13}C NMR (100 MHz, DMSO-d_6) δ 170.1, 168.2, 144.3, 103.1, 60.1, 36.9, 14.0. HRMS (ESI) calculated for C$_7$H$_{11}$N$_2$O$_2$S [M + H]$^+$ 187.0540, found 187.0547.

2-(2-(((Benzyloxy)carbonyl)amino)thiazol-4-yl)acetic acid (2). To a solution of ester **1** (3.72 g, 20 mmol) in 40 mL CH$_2$Cl$_2$, DMAP (4.88 g, 40 mmol) was added and stirred under ice cold conditions. After 10 min, benzylchoroformate (6.8 g, 40 mmol) was added. The reaction mixture was stirred overnight under argon. Next, 1 (N) HCl was added, and the reaction mixture was extracted by CH$_2$Cl$_2$ (3 × 20 mL), dried over Na$_2$SO$_4$, and evaporated in vacuum to obtain the crude product. The crude product was subsequently dissolved in 10 mL THF, and 2 (N) NaOH solution (10 mL) was added. After stirring at RT for 1.5 h, the reaction mixture was cooled at 0 °C and then acidified with 2 (N) aqueous HCl at pH ∼ 5. Compound **2** (5.31 g, 91%) was obtained as an off-white solid. ^{1}H NMR (500 MHz, DMSO-d_6): δ 11.81 (s$_b$, 1H), 7.91 (s, 1H), 7.41−7.35 (m, 5H), 6.92 (s, 1H), 5.22 (s, 2H), 3.55 (s, 2H). ^{13}C NMR (100 MHz, DMSO-d_6) δ 171.3, 159.1, 141.4, 140.4, 135.9, 128.9, 128.5, 128.5, 128.3, 127.9, 107.9, 63.1, 38.6. HRMS (ESI) calculated for C$_{13}$H$_{12}$N$_2$NaO$_4$S [M + Na]$^+$ is 315.0415, found 315.0416.

Ethyl-N-(2-Boc-aminoethyl)glycinate (3). Mono-boc-ethlleynediamine (3.0 g, 18.72 mmol) and K$_2$CO$_3$ (3.35 g, 24.34 mmol) were dissolved in ACN/CH$_2$Cl$_2$ (1:1) (30 mL). Ethylbromoacetate (2.1 mL, 18.72 mmol) in ACN (20 mL) was added to the reaction mixture dropwise under argon atmosphere. The reaction mixture was allowed to stir for 6 h. The organic layer was extracted with CH$_2$Cl$_2$ (3 × 20 mL) and dried over Na$_2$SO$_4$. The mixture was concentrated under vacuum, and the resulting crude product was purified by column chromatography to afford the PNA backbone **3** (3.6 g, 78%) as a thick yellow liquid. ^{1}H NMR (500 MHz, CDCl$_3$) δ 5.52 (s$_b$, 1H), 4.13 (q, *J* = 7.2 Hz, 2H), 3.49 (s, 2H), 3.13 (d, *J* = 4.3 Hz, 2H), 2.81 (t, *J* = 5.2 Hz, 2H), 2.02 (s$_b$, 1H), 1.41 (s, 9H), 1.24 (t, *J* = 7.6 Hz, 3H). ^{13}C NMR (125 MHz, DMSO-d_6): δ 171.5, 156.3, 60.9, 55.5, 53.8, 50.7, 48.9, 28.6, 14.3. HRMS (ESI) calculated for C$_{11}$H$_{23}$N$_2$O$_4$ [M + H]$^+$ 247.1658, found 247.1652.

Thiazole PNA Monomer (4). To a mixture of Cbz-protected thiazole amino acid **2** (3 g, 10.26 mmol) and ethyl-*N*-(2-boc-aminoethyl)glycinate **3** (2.53 g, 10.26 mmol) in 15 mL dry DMF was added HBTU (5.83 g, 15.39 mmol), the peptide coupling reagent. The mixture was allowed to stir until a homogeneous mixture was obtained. Then, triethylamine (2.86 mL, 20.52 mmol) was added. The mixture was stirred overnight. The organic layer was washed through extraction with a saturated NaHCO$_3$ solution (2 × 20 mL), with 1 (N) HCl solution (2 × 20 mL), and once with brine solution (10 mL). The reaction mixture was extracted with CH$_2$Cl$_2$ (3 × 20 mL), dried over Na$_2$SO$_4$, and evaporated in vacuum to afford the crude product, which was purified by column chromatography (SiO$_2$, 2% MeOH in CH$_2$Cl$_2$) to obtain the desired crude product. Then, the product underwent ester hydrolysis using LiOH-H$_2$O (951 mg, 22.7 mmol) in THF/MeOH/H$_2$O (3:3:1) (15 mL). The reaction mixture was stirred for 5 h at 0 °C and monitored by TLC. After completion of the reaction,

the solvent was dried under vacuum. The crude obtained was dissolved in a small amount of water. A dropwise addition of saturated $KHSO_4$ solution to the crude under cold conditions allowed the reaction mixture to get precipitated under acidic pH. The resulting solid precipitate was filtered and dried to afford the PNA monomer **4** (3.28 g, 65%) as a white solid. ^{1}H NMR (400 MHz, DMSO-d_6): δ 11.83 (s$_b$, 1H), 7.41−7.35 (m, 5H), 6.92 (s, 1H), 6.86 (s, 1H), 5.23 (s, 2H), 3.94 (s, 2H), 3.70 (s, 2H), 3.57 (s, 1H), 3.41 (t, J = 6.1 Hz, 1H), 3.30 (t, J = 6.5 Hz, 1H), 3.07 (dd, J = 25.0, 5.8 Hz, 2H), 1.36 (s, 9H). ^{13}C NMR (100 MHz, DMSO-d_6): δ 170.9, 169.9, 169.5, 159.0, 155.7, 153.7, 145.3, 136.0, 128.5, 128.2, 128.0, 109.2, 78.0, 66.8, 48.1, 47.4, 35.6, 28.2. HRMS (ESI) calculated for $C_{22}H_{28}N_4NaO_7S$ $[M + Na]^+$ 515.1576, found 515.1562.

Thiazole PNA Dimer (Thz-2). Using the procedure of solid-phase peptide synthesis,[35] thiazole dimer (**Thz-2**) was prepared from thiazole PNA monomer **4** (50 mg, 0.1 mmol) by using 4-methylbenzhydrylamine (4-MBHA) resin (100−200 mesh size) (40 mg) followed by coupling with 3-(dimethylamino)-propylamine and CBz deprotection. **Thz-2** was obtained as a yellow colored liquid (40.8 mg, 69%). ^{1}H NMR (400 MHz, DMSO-d_6) δ 11.81 (s, 2H), 8.09 (s, 1H), 8.02 (s, 1H), 6.91 (s, 1H), 6.87 (s, 1H), 5.21 (s, 6H), 4.08 (s, 2H), 3.92 (s, 3H), 3.73 (s, 4H), 3.67 (t, J = 7.1 Hz, 6H), 3.58 (t, J = 6.8 Hz, 3H), 3.15 (s$_b$, 2H), 2.26 (s, 6H). ^{13}C NMR (100 MHz, DMSO-d_6) δ 167.9, 167.7, 166.4, 165.9, 159.1, 153.7, 145.1, 135.9, 109.5, 66.8, 48.6, 45.7, 42.4, 38.3, 36.3, 36.2. HRMS (ESI) calculated for $C_{23}H_{39}N_{10}O_4S_2$ $[M + H]^+$ 583.2597, Found 583.2581.

Thiazole PNA Trimer (Thz-3). Using the procedure of solid phase synthesis,[35] the thiazole trimer (**Thz-3**) was prepared from thiazole PNA monomer **4** (50 mg, 0.1 mmol) by using 4-MBHA resin (40 mg) followed by coupling with 3-(dimethylamino)-propylamine and CBz deprotection. The compound **Thz-3** was obtained as a yellow liquid (51 mg, 61%). ^{1}H NMR (400 MHz, DMSO-d_6) δ 11.81 (s, 3H), 8.09 (s, 1H), 8.03−7.95 (m, 2H), 6.91 (s, 2H), 6.87 (s, 1H), 5.22 (s, 6H), 4.08 (s, 2H), 3.93 (s, 3H), 3.73 (s, 3H), 3.69−3.66 (m, 6H), 3.60−3.57 (m, 2H), 3.15 (s, 4H), 2.89 (s, 1H), 2.83 (s, 1H), 2.27 (s, 7H), 2.08 (s, 6H). ^{13}C NMR (100 MHz, DMSO-d_6) δ 167.9, 167.7, 166.4, 165.9, 164.6, 159.2, 153.7, 145.1, 136.0, 109.5, 66.8, 48.6, 45.7, 42.4, 38.3, 38.2, 36.3, 36.2, 30.7. HRMS (ESI) calculated for $C_{32}H_{50}N_{14}NaO_6S_3$ $[M + Na]^+$ 845.3098, Found 845.3094.

Cytidine PNA Trimer (Cyt-3). Using the procedure of solid phase synthesis,[36] cytidine trimer (**Cyt-3**) was prepared from F-moc-C(Bhoc)-Aeg-OH (70 mg, 0.1 mmol) using RA-MBHA resin (40 mg) followed by coupling with 3-(dimethylamino)-propylamine. The desired product **Cyt-3** was obtained as a pale orange liquid (65.5 mg, 77%). ^{1}H NMR (400 MHz, DMSO-d_6) δ 7.86 (d, J = 6.4 Hz, 1H), 7.45 (d, J = 6.8 Hz, 2H), 7.37 (t, J = 7.4 Hz, 4H), 7.30 (s, 1H), 7.04 (s$_b$, 2H), 6.94 (s$_b$, 1H), 5.62 (d, J = 7.3 Hz, 2H), 4.35 (s, 3H), 4.13 (s, 8H), 3.77 (s, 3H), 3.55−3.53 (m, 4H), 2.94−2.92 (m, 4H), 2.82 (s, 7H), 2.67 (s, 5H), 2.33 (s, 6H). ^{13}C NMR (100 MHz, DMSO-d_6) δ 169.5, 162.3, 160.9, 153.8, 145.9, 109.7, 66.8, 54.7, 54.4, 48.6, 42.5, 42.4, 41.7, 38.2, 35.8, 30.8, 24.4. HRMS (ESI) calculated for $C_{35}H_{54}N_{17}O_9$ $[M + H]^+$ 856.4290, Found 856.4277.

Fluorimetric Titration. PNA oligomers (**Thz-2**, **Thz-3**, and **Cyt-3**) were diluted in filtered and degassed Tris-KCl buffer (100 mmol Tris KCl buffer, pH ∼ 7.4) to a final concentration of 1 μM. Fluorescence titrations were performed with

successive addition of preannealed DNA into the solution. The fluorescence spectra were recorded on a Horiba Jobin Yvon Fluoromax 3 instrument at 25 °C in a 10 mm path-length quartz cuvette with filtered 100 mM Tris-KCl buffer (pH ∼ 7.4). The DNA sequences (5′ → 3′) used in fluorimetric titrations are as follows:

c-MYC: $TG_4AG_3TG_4AG_3TG_3GAAGG$
scr-DNA: $CTG_2A_3GAGTGA_2GAGAGAGTGA_2GA_2G_2T_2AGCG_2$
BCL2: $AG_4CG_3CGCG_3AG_2AAG_5CG_3AGCG_4CTG$
h-TELO: $TTAG_3TTAG_3TTAG_3TTAG_3TTA$
ds-DNA: $CAATCG_2ATCGAATTCGATCCGATTG$

F is the fluorescence intensity, F_{max} is the maximum fluorescence intensity, F_0 is the fluorescence intensity in the absence of DNA, and K_d is the dissociation constant. All the binding constants of fluorescence spectral data have been calculated using the following Hill equation with the help of Origin Pro8.0:

$$F = F_0 + \frac{(F_{max} - F_0)[DNA]}{K_d + [DNA]}$$

FRET Melting Analysis. FRET melting assay has been performed according to a previously reported protocol.[37,38] Dual-labeled DNA sequences with a donor fluorophore 6-carboxyfluorescein (5′-FAM) and an acceptor fluorophore 6-carboxytetramethylrhodamine (3′-TAMRA) were used for the study. For FRET melting titration experiments, various concentrations of **Thz-2**, **Thz-3**, and **Cyt-3** (0−10 μM) were added to the preannealed dual-labeled DNA sequences (at 200 nM final concentration) in 60 mM potassium cacodylate buffer. The final solution was loaded in a Roche 96-well plate and incubated for 1 h. Measurements were made in triplicate with an excitation wavelength of 483 nm and a detection wavelength of 533 nm using LightCycler 480-II System (Roche). Final analysis of the data was carried out using OriginPro 8.0 (OriginLab Corp.). Dual fluorescently labeled DNA oligonucleotides used in these experiments are as follows:

c-MYC: 5′ FAM-d $(TG_4AG_3TG_4AG_3TG_3GAAGG)$-TAMRA-3′
BCL2: 5′ FAM-d-$(AG_4CG_3CGCG_3AGGAAG_5CG_3AGCG_4CTG)$-TAMRA-3′
h-TELO: 5′ FAM-d $(TTAG_3TTAG_3TTAG_3TTAG_3TTA)$-TAMRA-3′
ds-DNA: 5′ FAM-d $(CAATCGGATCGAATTCGATCCGATTG)$ TAMRA-3′

Isothermal Calorimetry. This experiment was carried out with MICROCAL PEAQ-ITC (Malvern Instruments, Great Britain) at 25 °C. 300 μL of different G-quadruplex DNAs (*c-MYC*, *h-TELO*, *BCL2*) and dsDNA at 5 μM concentration in 100 mM Tris-KCl was loaded into the sample cell and the modified PNAs at 50 μM in the same buffer was prepared for titration. For a typical titration, 2 μL of ligand solution was injected into the sample cell with each G4 DNA at 150 s interval with a stirring speed of 750 rpm. Each injection lasted for 4 s, and 19 injections constituted the whole titration process. The K_d value was obtained through fitting the binding isotherms in MICROCAL PEAQ-ITC Analysis software.

Circular Dichroism Spectroscopy. CD titrations were performed in a Jasco J815 spectropolarimeter using a quartz cuvette of path length 1 mm at 25 °C. All the spectra were recorded in the wavelength range of 200−350 nm at a scan rate

of 200 nm/min and averaged over three scans. DNA sequences were preannealed in Tris-KCl buffer (100 mM KCl, 10 mM Tris-HCl, pH 7.4). The spectra were recorded after each successive addition of ligands (**Thz-2** and **Thz-3**) into 10 μM G4 solution. The final analysis of the recorded spectra was conducted using OriginPro 8.0 (OriginLab Corp.).

Molecular Dynamics Simulations. To computationally model the interaction between the *c-MYC* G4 DNA and **Thz-3** and identify the most probable interacting geometries, we performed classical molecular dynamics simulations with *c-MYC* and the **Thz-3** in 1:1 and 1:3 ratios. For the 1:1 case, seven different simulations with different initial structures were run. while for the 1:3 scenario, one long simulation was performed. To build the systems, the structure of *c-MYC* was obtained from the PDB ID: 2L7V, while the structure of **Thz-3** was built with the Gaussview visualizer followed by quantum chemistry optimization using density functional theory (DFT) at the B3LYP/6-31G** level of theory.[48−51] The composites of 1:1 initial configuration of *c-MYC* and **Thz-3** were prepared using the PACKMOL code.[52] All resulting structures were solvated in water boxes, the negative charges due to phosphate backbone were neutralized by adding potassium ions, and further KCl was added to make the overall concentration 0.1 M. The final size of the boxes was 7×7 nm^2. It is noteworthy that the box sizes were chosen such that the nucleic acid and **Thz-3** are non-interacting with their periodic images, having a minimum inter-replica distance of ~4 nm. Periodic boundary conditions were applied in all directions without any gap between periodic images. First, each of the systems was minimized for 10^5 steps while keeping the DNA atoms constrained by a harmonic force constant of 100 kcal/mol/Å^2, and another minimization was performed for 105 steps without any constraint. Then, the systems were equilibrated for 50 ns at 100 K in canonical (NVT) ensemble, again constraining the DNA atoms by a force constant of 100 kcal/mol/Å^2. Further, the force constant was reduced to 10 kcal/mol/Å^2, and heating was performed to 300 K over the period of 50 ns. Finally, constraining forces over DNA atoms were removed, and the systems were equilibrated for another 50 ns in isothermal−isobaric (NPT) ensemble at 300 K and 1 atmospheric pressure. Finally, production simulations were carried out with structures obtained at the end of the equilibration simulations at 300 K in NVT ensemble for 500 ns. A simulation box containing a single *c-MYC* was also built following the same protocol as mentioned above, and it was simulated for 300 ns in order to check the structural stability and evaluate the equilibrated structural characteristics of the G-4 DNA when no interacting molecules are present other than water. For the 1:3 simulation, a similar system building as well as minimization−equilibration protocol was followed, and the production simulation was performed for 1500 ns (1.5 μs).

For all simulations, isothermal conditions were maintained using Langevin dynamics with a damping coefficient of 5 ps^{-1}, and the Langevin piston method is used to maintain a pressure of 1 atm.[53] Constant pressure coupling was applied along all three directions, and for this purpose, a 100 fs piston period, 50 fs damping time constant, and 300 K piston temperatures are considered.[54] The particle mesh Ewald (PME) method with 1 Å grid is employed to calculate the periodic electrostatics, and a 2 fs time step is used to integrate classical equations of motion using the Velocity Verlet algorithm.[55] We used the SHAKE algorithm to hold rigid covalent bonds with hydrogen atoms.[56] Nonbonded interactions are calculated with a cutoff

distance of 12 Å, and atomic coordinates are stored after every 10 ps for the trajectory analysis. The NAMD 2.12 package was used for classical molecular dynamics simulations, VMD for visualization, and our in-house Tcl scripts as well as VMD plug-ins for the analysis of data.[57,58] We used the TIP3P model for water, CHARMM36 nucleic acid force field parameters for the *c-MYC* G4 DNA, and CHARMM general force field (CGenFF) parameters for **Thz-3**.[59,60] The partial charges for the **Thz-3** atoms were assigned by calculating the Mullikan charges by reoptimizing the B3LYP/6-31G** optimized **Thz-3** at the MP2/6-31G** level of theory in conjunction with the IEFPCM solvation model in water as solvent, in accordance with the CGenFF protocol.[61]

For analyses, contact between the G4 DNA and **Thz-3** was taken into account only if any of the **Thz-3** atoms is within a cutoff distance of 0.6 nm with respect to the DNA. A hydrogen bond is defined using the following geometric criteria: D−A distance ≤0.35 nm and D−H−A angle ≥1200, which have previously been utilized for the investigations concerning the simulations of single and double stranded DNA's as well as DNA quadruplexes with 2D materials.[62−64] Two nucleotide residues were considered to be π-stacked if the COM distances between the heavy atoms of the aromatic rings are ≤0.5 nm.[65] Radius of gyration of the nucleic acid was calculated according to the formula $R_g = \sqrt{\frac{1}{n}\sum_{i=0}^{n}|r_i^2 - r_{com}^2|}$. The binding free energy of the **Thz-3** molecule with *c-MYC* was calculated using the adaptive biasing force module as implemented in NAMD 2.12, taking the distance between the centers-of-mass of **Thz-3** and the *c-MYC* G4 as the reaction coordinate.[66] The starting structures for free-energy calculations were taken as the last frame of the 500-ns-long production simulations (1:1). During the free energy calculation, the center of mass of *c-MYC* was constrained by a mild force constant of 10 kcal/mol/Å^2. The total length of the reaction coordinate was divided into several windows of the length 1 Å, and each of the windows was further divided into smaller bins of 0.2 Å widths. Finally, for each of the windows, a 40-ns-long simulation was performed. To confirm the reproducibility, three sets of free energy calculations were performed, and the average is reported. All DFT calculations were performed using the Gaussian09 package.[67]

Cell Culture. Human cervical cancer (HeLa) cell and normal human kidney epithelial (NKE) cells were cultured in 10% fetal bovine serum (FBS) supplemented Dulbecco's modified Eagle's medium (DMEM) at 37 °C in 5% CO$_2$ containing humidified incubator.

Cell Viability Assay. HeLa and NKE cells were seeded in a 96-well plate (1×10^3 cells/well) and were treated with various concentrations of PNA **Thz-2**, **Thz-3**, and **Cyt-3** (Control, 1, 5, 10, 20, 50 μM). XTT (2,3-bis(2-methoxy-4-nitro-5-sulfophenyl)-*2H*-tetrazolium-5-carboxanilide) stock solution was prepared by mixing 4 mL (1 mg/ml) with 10 μL of the 10 mM phenazine methosulfate (PMS) solution. Following incubation with each compound for 24 h, 25 μL of XTT-PMS solution (1 mg/mL XTT+10 μL of 10 mM PMS) was added to each well. After incubation for 2 h at 37 °C, absorbance (A) of formazan dye was measured at 450 nm using an automated microplate reader. The percentage of viable cells was determined by calculating the (Absorbance of treated cells/ Absorbance of untreated cells) × 100. IC$_{50}$ values were determined with Origin Pro 8 software using nonlinear curve fitting.

Confocal Imaging. HeLa cells were seeded on glass coverslips placed in 6-well cell culture plates for 24 h followed by incubation with 5 μM **Thz-3** for 24 h in CO_2 (5%) incubator at 37 °C. After incubation, cells were washed with PBS three times to remove the excess ligand and fixed with 1:1 acetone−methanol mixture for 12 min at −20 °C. Cells were then very gently rinsed with PBS buffer three times, and the coverslips were mounted on glass slides having 20 μL NucRed Live647 ReadyProbe Reagent. The cellular localization of **Thz-3** was then monitored by imaging in Leica DMI8 Stellaris 5 microscope using green and red channels.

RNA Extraction and qRT-PCR Analysis. HeLa cells were treated with 5 μM and 10 μM of ligands **Thz-2** and **Thz-3** and incubated for 24 h. After 24 h, total RNA was extracted from ligand-treated and -untreated cells by using the Trizol kit according to the manufacturer's protocol (Invitrogen Corporation). Next, cDNA was prepared by using Verso cDNA Synthesis Kit. The thermal cycling condition was programmed at 42 °C for 30 min and at 95 °C for 2 min for one cycle. Using the cDNA library as the template, we carried out a quantitative real-time polymerase chain reaction (qRT-PCR) on a Light Cycler 480 II (Roche) with SYBR green JumpStart TaqReadyMix (Sigma, Saint Louis, USA) reagent. The primer sequences used for the qRT-PCR analyses are as follows:

18S rRNA (forward): 5′-GAT$_2$C$_2$GTG$_3$TG$_2$TG$_2$TGC-3′
18S rRNA (reverse): 5′-A$_2$GA$_2$GT$_2$G$_5$ACGCCGA-3′
c-MYC (forward): 5′-CTGCGACGAG$_2$AG$_2$AG$_2$ACT-3′
c-MYC (reverse): 5′-G$_2$CAGCAGCTCGA$_2$T$_3$C2-3′
BCL-2 (forward): 5′-GAG$_2$AT$_2$GTG$_2$C$_2$T$_2$CT$_3$G-3′
BCL-2 (reverse): 5′-GC$_2$G$_2$T$_2$CAG$_2$TACTCAGTC-3′

The comparative cycle threshold method (C_t method) for relative quantification of gene expression has been used. The C_t values of 18s rRNA were determined as endogenous control gene. ΔC_t of the treated and control were calculated from the C_t values. Finally, the arithmetic calibrator $2^{-\Delta(\Delta Ct)}$ was used to calculate the relative level of mRNA expression of the *c-MYC* and *BCL2* gene. Differences in *c-MYC* expression were expressed as fold changes.

Dual Luciferase Assay. HeLa cells were cultured in 6-well plates in DMEM media (10% FBS) and incubated overnight in 5% CO_2 incubator at 37 °C. For each well, 300 ng of *c-MYC* promoter (Del4) plasmid or *BCL2* (LB322) plasmid containing firefly luciferase plasmid and 30 ng of pRL-TK containing *Renilla* luciferase plasmid were diluted in incomplete DMEM and incubated at RT for 45 min along with Lipofectamine 2000 reagent. The cells were incubated with DNA:Lipofectamine solutions in incomplete media kept at 37 °C in 5% CO_2 for 6 h. After that, the cells were washed PBS and replenished with 2 mL DMEM (10% FBS) containing 5 μM and 10 μM of **Thz-2** and **Thz-3** and incubated at 37 °C in 5% CO_2 in the air for 40 h. Next, the cells were washed with PBS and lysed, and the levels of firefly and Renilla luciferase luminescence were measured using multimode ELISA plate reader. Ratios of firefly signal:Renilla signal (FF/RL) were calculated and normalized to ensure equal transfection.

■ ASSOCIATED CONTENT

Ⓢ Supporting Information

The Supporting Information is available free of charge at https://pubs.acs.org/doi/10.1021/acs.bioconjchem.2c00075.

Additional experimental results, ^{1}H and ^{13}C NMR spectra, HPLC chromatograms of the final compounds, reaction schemes, normalized fluorescence responses of ligands (PDF)

■ AUTHOR INFORMATION

Corresponding Author

Jyotirmayee Dash − *School of Chemical Sciences, Indian Association for the Cultivation of Science, Kolkata 700032, India;* ⓞ orcid.org/0000-0003-4130-2841; Email: ocjd@iacs.res.in

Authors

Ananta Gorai − *School of Chemical Sciences, Indian Association for the Cultivation of Science, Kolkata 700032, India*

Ritapa Chaudhuri − *School of Chemical Sciences, Indian Association for the Cultivation of Science, Kolkata 700032, India*

Titas Kumar Mukhopadhyay − *School of Chemical Sciences, Indian Association for the Cultivation of Science, Kolkata 700032, India;* ⓞ orcid.org/0000-0003-2505-6732

Ayan Datta − *School of Chemical Sciences, Indian Association for the Cultivation of Science, Kolkata 700032, India;* ⓞ orcid.org/0000-0001-6723-087X

Complete contact information is available at:
https://pubs.acs.org/10.1021/acs.bioconjchem.2c00075

Author Contributions

‡A.G. and R. C. contributed equally to this work.

Notes

The authors declare no competing financial interest.

■ REFERENCES

(1) Nielsen, P. E.; Egholm, M.; Berg, R. H.; Buchardt, O. Sequence-selective recognition of DNA by strand displacement with a thymine-substituted polyamide. *Science* **1991**, *254*, 1497−1500.

(2) Egholm, M.; Buchardt, O.; Christensen, L.; Behrens, C.; Freier, S. M.; Driver, D. A.; Berg, R. H.; Kim, S. K.; Norden, B.; Nielsen, P. E. PNA hybridizes to complementary oligonucleotides obeying the Watson−Crick hydrogen-bonding rules. *Nature* **1993**, *365*, 566−568.

(3) Lundin, K. E.; Good, L.; Strömberg, R.; Gräslund, A.; Smith, C. E. Biological activity and biotechnological aspects of peptide nucleic acid. *Adv. Genet.* **2006**, *56*, 1−51.

(4) Peffer, N. J.; Hanvey, J. C.; Bisi, J. E.; Thomson, S. A.; Hassman, C. F.; Noble, S. A.; Babiss, L. E. Strand-invasion of duplex DNA by peptide nucleic acid oligomers. *Proc. Natl. Acad. Sci. U. S. A.* **1993**, *90*, 10648−10652.

(5) Vickers, I. A.; Griffith, M. C.; Ramasamy, K.; Risen, L. M.; Freier, S. M. Inhibition of NF-κB specific transcriptional activation by PNA strand invasion. *Nucleic Acids Res.* **1995**, *23*, 3003−3008.

(6) Wittung, P.; Nielsen, P.; Nordén, B. Direct Observation of Strand Invasion by Peptide Nucleic Acid (PNA) into Double-Stranded DNA. *J. Am. Chem. Soc.* **1996**, *118*, 7049−7054.

(7) Marin, V. L.; Armitage, B. A. RNA guanine quadruplex invasion by complementary and homologous PNA probes. *J. Am. Chem. Soc.* **2005**, *127*, 8032−8033.

(8) Datta, B.; Schmitt, C.; Armitage, B. A. Formation of a PNA2−DNA2 hybrid quadruplex. *J. Am. Chem. Soc.* **2003**, *125*, 4111−4118.

(9) Ishizuka, T.; Yang, J.; Komiyama, M.; Xu, Y. G-rich sequence-specific recognition and scission of human genome by PNA/DNA hybrid G-quadruplex formation. *Angew. Chem., Int. Ed.* **2012**, *124*, 7310−7314.

(10) Paul, A.; Sengupta, P.; Krishnan, Y.; Ladame, S. Combining G-quadruplex targeting motifs on a ssingle peptide nucleic acid scaffold: a hybride (3 + 1) PNA-DNA bimolecular quadruplex. *Chem.—Eur. J.* **2008**, *14*, 8682−8689.

(11) Tan, D. J. Y.; Das, P.; Winnerdy, F. R.; Lim, K. W.; Phan, A. T. Guanine anchoring: a strategy for specific targeting of a G-quadruplex using short PNA, LNA and DNA molecules. *Chem. Commun.* **2020**, *56*, 5897−5900.

(12) Onyshchenko, M. I.; Gaynutdinov, T. I.; Englund, E. A.; Appella, D. H.; Neumann, R. D.; Panyutin, I. G. Stabilization of G-quadruplex in BCL2 promoter region in double-stranded DNA by invading short PNAs. *Nucleic Acids Res.* **2009**, *37*, 7570−7580.

(13) Tassinari, M.; Zuffo, M.; Nadai, M.; Pirota, V.; Montalvo, A. C. S.; Doria, F.; Freccero, M.; Richter, S. N. Selective targeting of mutually exclusive DNA G-quadruplexes: HIV-1 LTR as paradigmatic model. *Nucleic Acids Res.* **2020**, *48*, 4627−4642.

(14) Cadoni, E.; De Paepe, L.; Manicardi, A.; Madder, A. Beyond small molecules: targeting G-quadruplex structures with oligonucleotides and their analogues. *Nucleic Acids Res.* **2021**, *49*, 6638−6659.

(15) Debart, F.; Abes, S.; Deglane, G.; Moulton, H.; Clair, P.; Gait, M.; Vasseur, J.-J.; Lebleu, B. Chemical Modifications to Improve the Cellular Uptake of Oligonucleotides. *Curr. Top. Med. Chem.* **2007**, *7*, 727−737.

(16) Wolf, Y.; Pritz, S.; Abes, S.; Bienert, M.; Lebleu, B.; Oehlke, J. Structural requirements for cellular uptake and antisense activity of PNAs conjugated with various peptides. *Biochemistry.* **2006**, *45*, 14944−14954.

(17) Zengeya, T.; Gupta, P.; Rozners, E. Triple-Helical Recognition of RNA Using 2-Aminopyridine-Modified PNA at Physiologically Relevant Conditions. *Angew. Chem., Int. Ed.* **2012**, *51*, 12593−12596.

(18) Brodyagin, N.; Kataoka, Y.; Kumpina, I.; McGee, D. W.; Rozners, E. Cellular uptake of 2-aminopyridine-modified peptide nucleic acids conjugated with cell-penetrating peptides. *Biopolymers* **2022**, *113*, e23484.

(19) Gasparello, J.; Manicardi, A.; Casnati, A.; Corradini, R.; Gambari, R.; Finotti, A.; Sansone, F. Efficient cell penetration and delivery of peptide nucleic acids by an argininocalix[4]arene. *Sci. Rep.* **2019**, *9*, 3036.

(20) Zhou, P.; Wang, M.; Du, L.; Fisher, G. W.; Waggoner, A.; Ly, D. H. Novel Binding and Efficient Cellular Uptake of Guanidine-Based Peptide Nucleic Acids (GPNA). *J. Am. Chem. Soc.* **2003**, *125*, 6878−6879.

(21) Turner, J. J.; Ivanova, G. D.; Verbeure, B.; Williams, D.; Arzumanov, A. A.; Abes, S.; Lebleu, B.; Gait, M. J. Cell-penetrating peptide conjugates of peptide nucleic acids (PNA) as inhibitors of HIV-1 Tat-dependent trans-activation in cells. *Nucleic Acids Res.* **2005**, *33*, 6837−6849.

(22) Padroni, G.; Parkinson, J. A.; Fox, K. R.; Burley, G. A. Structural basis of DNA duplex distortion induced by thiazole-containing hairpin polyamides. *Nucleic Acids Res.* **2018**, *46*, 42−53.

(23) Tera, M.; Ishizuka, H.; Takagi, M.; Suganuma, M.; Shin-ya, K.; Nagasawa, K. Macrocyclic Hexaoxazoles as Sequence- and Mode-Selective G-Quadruplex Binders. *Angew. Chem., Int. Ed.* **2008**, *47*, 5557−5560.

(24) Neidle, S. Quadruplex nucleic acids as targets for anticancer therapeutics. *Nat. Rev. Chem.* **2017**, *1*, 1.

(25) Bochman, M. L.; Paeschke, K.; Zakian, V. A. DNA secondary structures: stability and function of G-quadruplex structures. *Nat. Rev. Genet.* **2012**, *13*, 770−780.

(26) Carvalho, J.; Mergny, J. L.; Salgado, G. F.; Queiroz, J. A.; Cruz, C. G-quadruplex, Friend or Foe: The Role of the G-quartet in Anticancer Strategies. *Trends Mol. Med.* **2020**, *26*, 848−86.

(27) Varshney, D.; Spiegel, J.; Zyner, K.; Tannahill, D.; Balasubramanian, S. The regulation and functions of DNA and RNA G-quadruplexes. *Nat. Rev. Mol. Cell Biol.* **2020**, *21*, 459−474.

(28) Siddiqui-Jain, A.; Grand, C. L.; Bearss, D. J.; Hurley, L. H. Direct evidence for a G-quadruplex in a promoter region and its targeting with a small molecule to repress *c-MYC* transcription. *Proc. Natl. Acad. Sci. U.S.A.* **2002**, *99*, 11593−11598.

(29) Balasubramanian, S.; Hurley, L. H.; Neidle, S. Targeting G-quadruplexes in gene promoters: a novel anticancer strategy? *Nat. Rev. Drug Discovery* **2011**, *10*, 261−275.

(30) Phan, A. T.; Modi, Y. S.; Patel, D. J. Propeller-Type Parallel-Stranded G-Quadruplexes in the Human *c-myc* Promoter. *J. Am. Chem. Soc.* **2004**, *126*, 8710−8716.

(31) Gonzalez, V.; Hurley, L. H. The c-MYC NHE III1: function and regulation. *Annu. Rev. Pharmacol. Toxicol.* **2010**, *50*, 111−129.

(32) Dutta, D.; Debnath, M.; Müller, D.; Paul, R.; Das, T.; Bessi, I.; Schwalbe, H.; Dash, J. Cell penetrating thiazole peptides inhibit *c-MYC* expression via site-specific targeting of *c-MYC* G-quadruplex. *Nucleic Acids Res.* **2018**, *46*, 5355−5365.

(33) Zhai, Q.; Gao, C.; Ding, J.; Zhang, Y.; Islam, B.; Lan, W.; Hou, H.; Deng, H.; Li, J.; Hu, Z.; Mohamed, H.-I.; Xu, S.; Cao, C.; Haider, S.-M.; Wei, D. Selective recognition of c-MYC Pu22 G-quadruplex by a fluorescent probe. *Nucleic Acids Res.* **2019**, *47*, 2190−2204.

(34) Calabrese, D. R.; Chen, X.; Leon, E. C.; Gaikwad, S. M.; Phyo, Z.; Hewitt, W. M.; Alden, S.; Hilimire, T. A.; He, F.; Michalowski, A. M.; Simmons, J. K.; Saunders, L. B.; Zhang, S.; Connors, D.; Walters, K. J.; Mock, B. A.; Schneekloth, J. S., Jr. Chemical and structural studies provide a mechanistic basis for recognition of the MYC G-quadruplex. *Nat. Commun.* **2018**, *9*, 4229.

(35) Komiyama, M.; Aiba, Y.; Ishizuka, T.; Sumaoka, J. Solid-phase synthesis of pseudo-complementary peptide nucleic acids. *Nat. Protoc.* **2008**, *3*, 646−654.

(36) Coin, I.; Beyermann, M.; Bienert, M. Solid-phase peptide synthesis: from standard procedures to the synthesis of difficult sequences. *Nat. Protoc.* **2007**, *2*, 3247−3256.

(37) De Cian, A.; Guittat, L.; Kaiser, M.; Saccà, B.; Amrane, S.; Bourdoncle, A.; Alberti, P.; Teulade-Fichou, M.-P.; Lacroix, L.; Mergny, J.-L. Fluorescence-based melting assays for studying quadruplex ligands. *Methods* **2007**, *42*, 183−195.

(38) Mergny, J. L.; Lacroix, L.; Teulade-Fichou, M. P.; Hounsou, C.; Guittat, L.; Hoarau, M.; Arimondo, P. B.; Vigneron, J. P.; Lehn, J. M.; Riou, J. F.; Garestier, T. Telomerase inhibitors based on quadruplex ligands selected by a fluorescence assay. *Proc. Natl. Acad. Sci. USA* **2001**, *98*, 3062−3067.

(39) Dai, J.; Carver, M.; Hurley, L. H.; Yang, D. Solution structure of a 2:1 quindoline−*c-MYC* G-quadruplex: insights into G-quadruplex-interactive small molecule drug design. *J. Am. Chem. Soc.* **2011**, *133*, 17673−17680.

(40) Wang, M.; Mao, Z.; Kang, T.-S.; Wong, C.-Y.; Mergny, J.-L.; Leung, C.-H.; Ma, D.-L. Conjugating a groove-binding motif to an Ir(III) complex for the enhancement of G-quadruplex probe behavior. *Chem. Sci.* **2016**, *7*, 2516−2523.

(41) Nanjunda, R.; Musetti, C.; Kumar, A.; Ismail, M. A.; Farahat, A. A.; Wang, S.; Sissi, C.; Palumbo, M.; Boykin, D. W.; Wilson, W. D. Heterocyclic Dications as a New Class of Telomeric G-Quadruplex Targeting Agents. *Curr. Pharm. Des.* **2012**, *18*, 1934−1947.

(42) Ma, D.-L.; Chan, D. S. -H.; Fu, W.-C.; He, H.-Z.; Yang, H.; Yan, S.-C.; Leung, C.-H. Discovery of a Natural Product-Like *c-myc* G-Quadruplex DNA Groove-Binder by Molecular Docking. *PLoS One* **2012**, *7*, e43278.

(43) Huang, J.; Li, G.; Wu, Z.; Song, Z.; Zhou, Y.; Shuai, L.; Weng, X.; Zhou, X.; Yang, G. Bisbenzimidazole to benzobisimidazole: from binding B-form duplex DNA to recognizing different modes of telomere G-quadruplex. *Chem. Commun.* **2009**, 902−904.

(44) Jain, A. K.; Bhattacharya, S. Interaction of G-Quadruplexes with Nonintercalating Duplex-DNA Minor Groove Binding Ligands. *Bioconjugate Chem.* **2011**, *22*, 2355−2368.

(45) Krishna, M. S.; Wang, Z.; Zheng, L.; Bowry, J.; Ong, A. A. L.; Mu, Y.; Prabakaran, M.; Chen, G. *Biochemistry* **2019**, *58*, 3777.

(46) OliPass PNA; https://www.olipass.com/front/eng/competitive/technology.do.

(47) Karuvalam, R. P.; Haridas, K. R.; Nayak, S. K.; Guru Row, T. N.; Rajeesh, P.; Rishikesan, R.; Kumari, N. S. Design, synthesis of some new (2-aminothiazol-4-yl)methylester derivatives as possible antimicrobial and antitubercular agents. *Eur. J. Med. Chem.* **2012**, *49*, 172−182.

(48) Becke, A. D. Density-functional thermochemistry. III. The role of exact exchange. *J. Chem. Phys.* **1993**, *98*, 5648−5652.

(49) Stephens, P. J.; Devlin, F. J.; Chabalowski, C. F.; Frisch, M. J. Ab Initio Calculation of Vibrational Absorption and Circular Dichroism Spectra Using Density Functional Force Fields. *J. Phys. Chem. C* **1994**, *98*, 11623−11627.

(50) Lee, C.; Yang, W.; Parr, R. G. Development of the Colle-Salvetti correlation-energy formula into a functional of the electron density. *Phys. Rev.* **1988**, *37*, 785−789.

(51) Ditchfield, R.; Hehre, W. J.; Pople, J. A. Self-Consistent Molecular-Orbital Methods. IX. An Extended Gaussian-Type Basis for Molecular-Orbital Studies of Organic Molecules. *J. Chem. Phys.* **1971**, *54*, 724−728.

(52) Martínez, L.; Andrade, R.; Birgin, E. G.; Martínez, J. M. PACKMOL: A package for building initial configurations for molecular dynamics simulations. *J. Comput. Chem.* **2009**, *30*, 2157−2164.

(53) Martyna, G. J.; Tobias, D. J.; Klein, M. L. Constant pressure molecular dynamics algorithms. *J. Chem. Phys.* **1994**, *101*, 4177−4189.

(54) Feller, S. E.; Zhang, Y.; Pastor, R. W.; Brooks, B. R. Constant pressure molecular dynamics simulation: The Langevin piston method. *J. Chem. Phys.* **1995**, *103*, 4613−4621.

(55) Darden, T.; York, D.; Pedersen, L. Particle mesh Ewald: An N·log (N) method for Ewald sums in large systems. *J. Chem. Phys.* **1993**, *98*, 10089−10092.

(56) Andersen, H. C. Rattle: A "velocity" version of the shake algorithm for molecular dynamics calculations. *J. Comput. Phys.* **1983**, *52*, 24−34.

(57) Kalé, L.; Skeel, R.; Bhandarkar, M.; Brunner, R.; Gursoy, A.; Krawetz, N.; Phillips, J.; Shinozaki, A.; Varadarajan, K.; Schulten, K. NAMD2: Greater Scalability for Parallel Molecular Dynamics. *J. Comput. Phys.* **1999**, *151* (1), 283−312.

(58) Humphrey, W.; Dalke, A.; Schulten, K. VMD: Visual molecular dynamics. *J. Mol. Graph.* **1996**, *14*, 33−38.

(59) Jorgensen, W. L.; Chandrasekhar, J.; Madura, J. D.; Impey, R. W.; Klein, M. L. Comparison of simple potential functions for simulating liquid water. *J. Chem. Phys.* **1983**, *79*, 926−935.

(60) Vanommeslaeghe, K.; Hatcher, E.; Acharya, C.; Kundu, S.; Zhong, S.; Shim, J.; Darian, E.; Guvench, O.; Lopes, P.; Vorobyov, I.; Mackerell, A. D., Jr CHARMM general force field: A force field for drug-like molecules compatible with the CHARMM all-atom additive biological force fields. *J. Comput. Chem.* **2009**, *31*, 671−690.

(61) Møller, C.; Plesset, M. S. Note on an Approximation Treatment for Many-Electron Systems. *Phys. Rev.* **1934**, *46*, 618−622.

(62) Mukhopadhyay, T. K.; Bhattacharyya, K.; Datta, A. Gauging the Nanotoxicity of h2D-C2N toward Single-Stranded DNA: An in Silico Molecular Simulation Approach. *ACS Appl. Mater. Interfaces* **2018**, *10*, 13805−13818.

(63) Mukhopadhyay, T. K.; Datta, A. Screening two dimensional materials for the transportation and delivery of diverse genetic materials. *Nanoscale* **2020**, *12*, 703−719.

(64) Mukhopadhyay, T. K.; Datta, A. Delicate Balance of Non-Covalent Forces Govern the Biocompatibility of Graphitic Carbon Nitride towards Genetic Materials. *ChemPhysChem.* **2020**, *21*, 1836−1846.

(65) Mukhopadhyay, T.; Datta, A. Design Rules for the Generation of Stable Quartet Phases of Nucleobases over 2D Materials. *J. Phys. Chem. C* **2018**, *122*, 28918−28933.

(66) Darve, E.; Rodríguez-Gómez, D.; Pohorille, A. Adaptive biasing force method for scalar and vector free energy calculations. *J. Chem. Phys.* **2008**, *128*, 144120.

(67) Frisch, M. J.; Trucks, G. W.; Schlegel, H. B.; Scuseria, G. E.; Robb, M. A.; Cheeseman, J. R.; Scalmani, G.; Barone, V.; Mennucci, B.; Petersson, G. A.; Nakatsuji, H.; Caricato, M.; Li, X.; Hratchian, H. P.; Izmaylov, A. F.; Bloino, J.; Zheng, G.; Sonnenberg, J. L.; Hada, M.; Ehara, M.; Toyota, K.; Fukuda, R.; Hasegawa, J.; Ishida, M.; Nakajima, T.; Honda, Y.; Kitao, O.; Nakai, H.; Vreven, T.; Montgomery, J. A.; Peralta, Jr., J. E.; Ogliaro, F.; Bearpark, M.; Heyd, J. J.; Brothers, E.; Kudin, K. N.; Staroverov, V. N.; Keith, T.; Kobayashi, R.; Normand, J.; Raghavachari, K.; Rendell, A.; Burant, J. C.; Iyengar, S. S.; Tomasi, J.; Cossi, M.; Rega, N.; Millam, J. M.; Klene, M.; Knox, J. E.; Cross, J. B.; Bakken, V.; Adamo, C.; Jaramillo, J.; Gomperts, R.; Stratmann, R. E.; Yazyev, O.; Austin, A. J.; Cammi, R.; Pomelli, C.; Ochterski, J. W.; Martin, R. L.; Morokuma, K.; Zakrzewski, V. G.; Voth, G. A.; Salvador, P.; Dannenberg, J. J.; Dapprich, S.; Daniels, A. D.; Farkas, O.; Foresman, J. B.; Ortiz, J. V.; Cioslowski, J.; Fox, D. J. *Gaussian 09*; Gaussian, Inc., Wallingford, CT, 2010.

📖 Recommended by ACS